NRC Publications Archive
Archives des publications du CNRC

Finite element simulations of the thermomechanically coupled responses of thermal barrier coating systems using an unconditionally stable staggered approach

Li, Zhao; Chen, Kuiying; Jin, Tao

This publication could be one of several versions: author’s original, accepted manuscript or the publisher’s version. / La version de cette publication peut être l’une des suivantes : la version prépublication de l’auteur, la version acceptée du manuscrit ou la version de l’éditeur.

For the publisher’s version, please access the DOI link below./ Pour consulter la version de l’éditeur, utilisez le lien DOI ci-dessous.

Publisher’s version / Version de l'éditeur:
https://doi.org/10.1016/j.apm.2024.115750
Applied Mathematical Modelling, 138, PA, 2024-10-09

NRC Publications Archive Record / Notice des Archives des publications du CNRC :
https://nrc-publications.canada.ca/eng/view/object/?id=0393eba3-0ad3-470e-b07a-11aac360fac2
https://publications-cnrc.canada.ca/fra/voir/objet/?id=0393eba3-0ad3-470e-b07a-11aac360fac2

Access and use of this website and the material on it are subject to the Terms and Conditions set forth at
https://nrc-publications.canada.ca/eng/copyright
READ THESE TERMS AND CONDITIONS CAREFULLY BEFORE USING THIS WEBSITE.

L’accès à ce site Web et l’utilisation de son contenu sont assujettis aux conditions présentées dans le site
https://publications-cnrc.canada.ca/fra/droits
LISEZ CES CONDITIONS ATTENTIVEMENT AVANT D’UTILISER CE SITE WEB.

Questions? Contact the NRC Publications Archive team at PublicationsArchive-ArchivesPublications@nrc-cnrc.gc.ca. If you wish to email the authors directly, please see the first page of the publication for their contact information.

Vous avez des questions? Nous pouvons vous aider. Pour communiquer directement avec un auteur, consultez la première page de la revue dans laquelle son article a été publié afin de trouver ses coordonnées. Si vous n’arrivez pas à les repérer, communiquez avec nous à PublicationsArchive-ArchivesPublications@nrc-cnrc.gc.ca.

National Research Council Canada
Conseil national de recherches Canada

Applied Mathematical Modelling 138 (2025) 115750

Contents lists available at ScienceDirect

Applied Mathematical Modelling

journal homepage: www.elsevier.com/locate/apm

Finite element simulations of the thermomechanically coupled responses of thermal barrier coating systems using an unconditionally stable staggered approach

Zhao Li [a], Kuiying Chen [b], Tao Jin [a,*]

[a] Department of Mechanical Engineering, University of Ottawa, Ottawa, K1N 6N5, Ontario, Canada
[b] Structures and Materials Performance Laboratory, Aerospace Research Centre, National Research Council Canada, Ottawa, K1A 0R6, Ontario, Canada

ARTICLE INFO

Dataset link: https://github.com/taojinllnl/SmallDeformationThermoMechanicalCoupling

Keywords:
Thermomechanical coupling
Thermal barrier coating
Fractional step method
Operator split
Unconditional stability

ABSTRACT

Thermal barrier coating (TBC) systems have long been used in many engineering applications, such as jet engines and gas turbines. One pressing task is to evaluate their performance and integrity under long-term thermal cycles. This task requires an accurate and efficient time integration technique that is unconditionally stable, since large time steps are required to simulate TBC systems under long-term thermal effects. In this work, we present in detail several numerical methods to model the thermomechanically coupled responses of TBC systems, including a monolithic approach and two staggered approaches based on the isothermal split and the adiabatic split, respectively. We also demonstrate several finite element simulation techniques, such as the periodic boundary conditions and the adaptive mesh refinement, in the modeling of TBC systems. Through several numerical examples, we show that the staggered approach based on the adiabatic split preserves the unconditional stability of individual time integration techniques used for the mechanical phase and the thermal phase of the coupled problem. Moreover, the computational cost is significantly lower compared to the monolithic approach. This work provides an efficient time integration approach to model more complex behaviors of TBC systems under long-term thermal cycles.

1. Introduction

Thermal barrier coating (TBC) system is an essential component in jet engines and power generation gas turbines that operate in a demanding high-temperature environment for more efficient performance as well as reduced emission and noise [1]. TBC is a highly complex multi-layer metal-ceramic system. Due to the low thermal conductivity of the ceramic layer, TBC is capable to reduce the surface temperature of the underlying super-alloy structures and thus prolong the lifespan of the entire engine or turbine system.

A TBC system typically consists of four components from the outside towards inside of the protected part [1–4]: a ceramic top coat (TC) layer made of low thermal conductivity materials providing thermal protection by reducing heat flow to the underlying substrate, a thermally grown oxide (TGO) layer made of dense aluminum oxide and retarding subsequent oxidation, a bond coat (BC) layer increasing adhesion strength and reducing thermal expansion mismatch between the ceramic TC and the metallic substrate, and

---

* Corresponding author.
E-mail address: tao.jin@uottawa.ca (T. Jin).

https://doi.org/10.1016/j.apm.2024.115750
Received 23 May 2024; Received in revised form 6 September 2024; Accepted 2 October 2024

a super-alloy substrate layer, commonly nickel-based or cobalt-based, carrying mechanical loads. The chemical components of a TBC system are quite complex. For instance, the top coat (TC) ceramic layer typically has 10 - 25% porosity and is composed of zirconia (ZrO_2) partially stabilized with ∼6 - 8 wt-% yttria (Y_2O_3), generally referred as YSZ, 7YSZ or 6-8YSZ. The bond coat (BC) layer is mainly formed by 100 - 200 μm thick two phase overlay $\gamma+\beta$ MCrAlX (M can be Ni, Co or combination of them, and X represents Y, Hf, Si or other minor additives such as Re), for instance, NiCoCrAlY, or single phase β - NiAl or Pt modified β-NiAl (thickness is limited to ∼40 - 60 μm). In addition, the thermally grown oxide (TGO) layer is typically composed of <10 μm thick α-Al_2O_3 scale sourced from oxidization of aluminum in BC when exposed over 700 °C [5,6]. Generally speaking, the oxidation resistance of the TGO layer is protective for underlying layers, because TGO can delay the diffusion of the cations and oxygen by functioning as a barrier, but also reduce the infiltration of molten salt and the corrosion of the underlying substrate [6]. Moreover, Ramesh et al. [7] reported that the bonding strength, hardness, corrosion, and oxidation resistance of YSZ with Al_2O_3 are enhanced compared to the one with YSZ alone. On the other hand, during service under high temperature, the increasing thickness of TGO by further oxidation generally can be considered as an important factor resulting in failure and limiting the lifespan of TBCs [8]. Due to the formation of TGO, the adhesive strength of the bond coat (BC) decreases, and the thermal stress due to the mismatch of thermal expansion coefficients between the top coat (TC) and TGO increases [7].

TBC systems are commonly deposited by one of the two processes, the electron beam physical vapor deposition (EB-PVD) process that is typically used on dynamic parts of jet turbine engines, or the air plasma spray (APS) process that is typically used on stationary parts of gas turbine engines [9,10]. The typical micro-structures of EB-PVD and APS TBCs are different: the EB-PVD TBCs exhibit vertical columnar, micron-sized width (∼2 - 10 μm) structure, while the APS TBCs have porous and lamellar structure as well as overlapping splats composed parallel to the substrate [11]. More recently, the APS-based suspension plasma spray (SPS) shows great promises to replace the EB-PVD for turbine blades due to its lower cost and versatility [12]. Some micro-structures of SPS TBCs are similar to the ones of ASP TBCs.

Numerical simulation, especially the finite element method (FEM), provides an effective tool to evaluate the overall performance of the TBC systems under various environmental and operating conditions, and more importantly, investigate the potential failure mechanisms that are multi-physics and multi-scale processes [13–16]. There are many research efforts in the literature focusing on applying different numerical techniques to study the TBC systems. Through a finite element analysis, Shi et al. [17] reported that the concentration of the tensile stress normal to the TGO/BC interface may lead to the delamination or spallation of the TBC. Lee et al. [18] employed the FEM to investigate the impact of residual stress by considering the quenching stresses during the plasma spraying deposition of TBCs followed by cooling down to the room temperature. They showed that the residual stress concentration occurred at the interfaces between dissimilar materials, and the residual stress was greater at the TC/BC interface than the one at the BC/substrate interface. Nayebpashaee et al. [19] constructed a micro-mechanical based FEM from the SEM images to simulate the residual stress distribution and the fracture mode. Simulation of fracture initiation and propagation in the TBC systems is another important topic [20]. The typical numerical techniques include the virtual crack closure technique [21,22], the cohesive zone method [23–25], the extended finite element method [26], and the phase-field model [27–29]. More recently, machine learning is applied to predict the thermal conductivity in the TBC systems [30].

In order to evaluate the long-term performance and structural integrity of TBC systems, a computationally efficient and unconditionally stable time integration technique is essential to accurately simulate the thermomechanically coupled responses of TBC systems under cyclical thermal loading conditions. In this paper, we focus on accomplishing the following two tasks. First, we present in detail the numerical techniques used to simulate the thermomechanically coupled responses of TBC systems, including the finite element discretization and the time integration techniques derived from a monolithic approach and two staggered approaches based on the isothermal split and the adiabatic split [31], respectively. The detailed presentations of individual block matrices in the assembled linear system can facilitate the development of the finite element procedure to simulate the transient behavior of the thermomechanically coupled system in any commercial or open-source finite element packages. Second, we apply the monolithic approach and the staggered approach to investigate the thermomechanically coupled behavior of the thermal barrier coating (TBC) systems. Particularly, we discuss about the impact of stiff boundary conditions and the technique of adaptive mesh refinement in the finite element simulation of TBC systems. We recognize that TBC systems are highly complex and may exhibit inelastic behaviors such as plasticity and fracture during operations. However, for the current purpose of this research, we exclusively focus on the thermoelastic responses in our finite element simulations. With the provided numerical examples, we aim to demonstrate the advantages of the staggered approach based on the adiabatic split, which not only preserves the unconditional stability of individual time integration techniques employed for the mechanical phase and the thermal phase, but also provides accurate numerical results with a significantly lower computational cost compared to the monolithic approach. These advantages are especially appealing for three-dimensional finite element simulations of TBC systems under long-term cyclic thermal loading conditions that have a large number of degrees of freedom and require large time steps.

The remaining paper is organized as follows. In Section 2, we provide the partial differential equations that govern the thermomechanically coupled system and the corresponding boundary and initial conditions. Then, we present the semi-discrete weak forms of the monolithic approach and the staggered approaches based on the isothermal split and the adiabatic split, which are subsequently discretized by different time integration techniques. Subsequently, we provide the detailed expression of each block matrix in the linear systems derived from the monolithic approach and the two staggered approaches, respectively, which are required by the finite element simulations of the subsequent numerical examples. In Section 3, we use a two-dimensional numerical example to demonstrate that the staggered approach based on the adiabatic split can provide accurate numerical results as the monolithic approach. Moreover, it preserves the unconditional stability of individual time integration techniques [31], such as the Crank-Nicolson method and the backward Euler method that are used in the mechanical and thermal phases, whereas the isothermal split is only conditionally stable. In Section 4, we apply the monolithic approach and the staggered approach based on the adiabatic split to investigate the thermomechanical response of a TBC system. Particularly, we discuss in detail about several simulation techniques, such as the periodic boundary conditions and the adaptive mesh refinement, in the context of the finite element simulation of the TBC system. By comparing the computational cost associated with different methods, we demonstrate the superior computational efficiency of the staggered approach based on the adiabatic split. In Section 5, we summarize the conclusions of this work and discuss about several avenues to further improve the presented method in the context of TBC finite element simulations, particularly for the damage and failure analysis of TBC systems under long-term cyclic thermal loading conditions. The numerical methods presented in this paper are implemented in deal.II [32], which is an open-source finite element library. In order to support the efforts of open-source software and reproducible research, all the source codes developed in this paper are hosted on GitHub.[1]

2. Computational framework and numerical implementations

In this section, we first introduce the partial differential equations (PDEs) along with the boundary conditions and initial conditions that govern the thermomechanically coupled material behaviors. Then, we illustrate a monolithic approach and two staggered approaches that are based on the so-called isothermal split and adiabatic split originally proposed by Armero and Simo [31]. In particular, we present in detail the finite element technique for the spatial discretization and various time integration techniques for the temporal discretization based on the above approaches, respectively. We explicitly provide the linear systems derived from each approach for the convenience of finite element implementations.

2.1. Governing equations

We consider a continuum body $\mathcal{B}$ occupying a region $\Omega \in \mathbb{R}^n$ undergoes a deformation and temperature change during a time interval $\mathcal{T} = [0, T]$. The primary unknowns of the continuum body $\mathcal{B}$ are the displacement field $\boldsymbol{u}(\boldsymbol{x}, t)$ and the temperature field $\Theta(\boldsymbol{x}, t)$, which are functions of both location $\boldsymbol{x} \in \Omega$ and time $t \in \mathcal{T}$. The governing partial differential equations (PDEs) can be derived from the balances of momentum and energy in thermodynamics, which are expressed as

$$\begin{cases} \rho \ddot{\boldsymbol{u}} = \operatorname{div} \boldsymbol{\sigma} + \rho \boldsymbol{b} \\ \Theta \dot{\eta} = -\operatorname{div} \boldsymbol{q} + r \end{cases} \quad \text{in} \quad \Omega \times [0, T], \tag{1}$$

where $\ddot{\boldsymbol{u}}$ represents the acceleration field, $\boldsymbol{\sigma}$ represents the Cauchy stress field, the symmetry of which indicates the balance of angular momentum, ρ is the material density, $\boldsymbol{b}$ represents the body force per unit mass, η represents the entropy per unit volume, $\boldsymbol{q}$ is the heat flux, and r is the heat source. We introduce a reference temperature Θ_{ref}, such that $\Theta = \vartheta + \Theta_{\text{ref}}$, where ϑ is the relative temperature field.

For the displacement field $\boldsymbol{u}$, the external boundary $\partial\Omega$ is decomposed into two disjoint parts $\Gamma_{\boldsymbol{u}}$ and $\Gamma_{\boldsymbol{t}}$, such that $\Gamma_{\boldsymbol{u}} \cup \Gamma_{\boldsymbol{t}} = \partial\Omega$ and $\Gamma_{\boldsymbol{u}} \cap \Gamma_{\boldsymbol{t}} = \emptyset$. Similarly, for the temperature field Θ, the external boundary $\partial\Omega$ is decomposed into two disjoint parts Γ_ϑ and $\Gamma_{\boldsymbol{q}}$, such that $\Gamma_\vartheta \cup \Gamma_{\boldsymbol{q}} = \partial\Omega$ and $\Gamma_\vartheta \cap \Gamma_{\boldsymbol{q}} = \emptyset$. The PDEs shown in Eq. (1) are subject to the following essential and natural boundary conditions

$$\begin{cases} \boldsymbol{u} = \hat{\boldsymbol{u}} \quad \text{on} \quad \Gamma_{\boldsymbol{u}} \times [0, T] \\ \vartheta = \hat{\vartheta} \quad \text{on} \quad \Gamma_\vartheta \times [0, T] \\ \boldsymbol{\sigma}\boldsymbol{n} = \hat{\boldsymbol{t}} \quad \text{on} \quad \Gamma_{\boldsymbol{t}} \times [0, T] \\ \boldsymbol{q}\boldsymbol{n} = \hat{q} \quad \text{on} \quad \Gamma_{\boldsymbol{q}} \times [0, T] \end{cases}$$

where $\hat{\boldsymbol{u}}$ and $\hat{\boldsymbol{t}}$ are the prescribed displacement field and the traction force field on $\Gamma_{\boldsymbol{u}}$ and $\Gamma_{\boldsymbol{t}}$, and $\hat{\vartheta}$ and $\hat{q}$ are the prescribed (relative) temperature field and the heat flux on Γ_ϑ and $\Gamma_{\boldsymbol{q}}$. Since the deformation and the temperature of the continuum body also depend on time, the following set of initial conditions are provided,

$$\begin{cases} \boldsymbol{u} = \boldsymbol{u}_0 \\ \dot{\boldsymbol{u}} = \boldsymbol{v}_0 \quad \text{in} \quad \bar{\Omega} \times \{0\}. \\ \vartheta = \vartheta_0 \end{cases}$$

The deformation of the continuum body is assumed to be small, and the following linear relationship between the displacement field $\boldsymbol{u}$ and the strain field ϵ is adopted,

$$\epsilon = \frac{\nabla \boldsymbol{u} + (\nabla \boldsymbol{u})^{\mathrm{T}}}{2} = \nabla^{(\mathrm{s})} \boldsymbol{u}.$$

For the heat conduction, we adopt the Fourier's law,

---

[1] https://github.com/taojinllnl/SmallDeformationThermoMechanicalCoupling.

$$\boldsymbol{q} = -\boldsymbol{\kappa}\boldsymbol{\nabla}\Theta = -\boldsymbol{\kappa}\boldsymbol{\nabla}\vartheta,$$

where $\boldsymbol{\kappa}$ is the thermal conductivity tensor.

For the thermomechanically coupled problem, the following free energy function is adopted to describe the material constitutive behavior,

$$\Psi(\boldsymbol{\epsilon}, \vartheta) = \frac{1}{2}\boldsymbol{\epsilon} : \mathbb{C} : \boldsymbol{\epsilon} - \vartheta \boldsymbol{m} : \boldsymbol{\epsilon} - \frac{1}{2}\frac{c}{\Theta_{\text{ref}}}\vartheta^2, \tag{2}$$

where $\mathbb{C}$ is the fourth-order material tensor representing the material mechanical behavior, $\boldsymbol{m}$ is a 2nd-order tensor representing the strength of the thermomechanical coupling, and c is the heat capacity ($c = c_{\text{s}}\rho$, where c_{s} is the specific heat capacity and ρ is the material density). Based on the basics of thermodynamics, we can obtain the Cauchy stress as

$$\boldsymbol{\sigma} = \frac{\partial \Psi}{\partial \boldsymbol{\epsilon}} = \mathbb{C} : \boldsymbol{\epsilon} - \vartheta \boldsymbol{m} \tag{3}$$

and the entropy that is work-conjugate to the temperature field as

$$\eta = -\frac{\partial \Psi}{\partial \Theta} = \boldsymbol{m} : \boldsymbol{\epsilon} + \frac{c}{\Theta_{\text{ref}}}\vartheta. \tag{4}$$

Using the above constitutive relationships and introducing the velocity $\boldsymbol{v}$ as an extra unknown field, we recast the governing PDEs as

$$\begin{cases} \dot{\boldsymbol{u}} = \boldsymbol{v} \\ \dot{\boldsymbol{v}} = \dfrac{1}{\rho}\operatorname{div}(\mathbb{C} : \boldsymbol{\epsilon} - \vartheta \boldsymbol{m}) + \boldsymbol{b} \\ \dot{\vartheta} = \dfrac{1}{\bar{c}}\operatorname{div}(\bar{\boldsymbol{\kappa}}\boldsymbol{\nabla}\vartheta) - \dfrac{1}{\bar{c}}\boldsymbol{m} : \boldsymbol{\nabla}\boldsymbol{v} + \dfrac{r}{c} \end{cases} \quad \text{in} \quad \Omega \times [0, T], \tag{5}$$

where $\bar{c} = c/\Theta_{\text{ref}}$ and $\bar{\boldsymbol{\kappa}} = \boldsymbol{\kappa}/\Theta_{\text{ref}}$. In order to numerically solve the above coupled PDEs, we adopt the method of lines (an alternative approach is the Rothe's method). That is, we first use the finite element method to discretize the spatial domain and obtain a set of semi-discrete ordinary differential equations (ODEs). Then, we solve these ODEs via certain time integration techniques. We use $\delta\boldsymbol{u}$ for the test function of the displacement field, $\delta\boldsymbol{v}$ for the test function of the velocity field, and $\delta\vartheta$ for the temperature field, respectively. During a typical time step $[t_n, t_{n+1}]$, where $\Delta t = t_{n+1} - t_n$ is the time increment, we use $(\cdot)^{(n)}$ to represent quantities at the beginning of the time step that are assumed to be known, and $(\cdot)^{(n+1)}$ to represent quantities at the end of the time step that need to be solved.

2.2. Monolithic approach

For the monolithic approach, we obtain the unknowns $\{\boldsymbol{v}, \boldsymbol{u}, \vartheta\}^{(n+1)}$ by solving the fully coupled linear system simultaneously. To derive the fully coupled linear system, we first use the finite element method to discretize the spatial domain. We multiply the test functions $\{\delta\boldsymbol{v}, \delta\boldsymbol{u}, \delta\vartheta\}$ on both sides of the governing PDEs,

$$\begin{cases} (\delta\boldsymbol{v}, \dot{\boldsymbol{u}}) = (\delta\boldsymbol{v}, \boldsymbol{v}) \\ (\delta\boldsymbol{u}, \dot{\boldsymbol{v}}) = \left(\delta\boldsymbol{u}, \dfrac{1}{\rho}\operatorname{div}(\mathbb{C} : \boldsymbol{\epsilon} - \vartheta\boldsymbol{m})\right) + (\delta\boldsymbol{u}, \boldsymbol{b}) \\ \left(\delta\vartheta, \dot{\vartheta}\right) = \left(\delta\vartheta, \dfrac{1}{\bar{c}}\operatorname{div}(\bar{\boldsymbol{\kappa}}\boldsymbol{\nabla}\vartheta)\right) - \left(\delta\vartheta, \dfrac{1}{\bar{c}}\boldsymbol{m} : \boldsymbol{\nabla}\boldsymbol{v}\right) + \left(\delta\vartheta, \dfrac{r}{c}\right) \end{cases} \tag{6}$$

where

$$(\cdot, \cdot) = \int_{\Omega^{(e)}} (\cdot)(\cdot)\mathrm{d}V$$

stands for the bilinear form of the element integration.

Following the standard procedures such as integration by parts and the divergence theorem, we obtain the following weak form

$$\begin{cases} (\delta\boldsymbol{v}, \dot{\boldsymbol{u}}) = (\delta\boldsymbol{v}, \boldsymbol{v}) \\ (\delta\boldsymbol{u}, \dot{\boldsymbol{v}}) + \left(\boldsymbol{\nabla}\delta\boldsymbol{u}, \dfrac{1}{\rho}(\mathbb{C} : \boldsymbol{\epsilon} - \vartheta\boldsymbol{m})\right) = (\delta\boldsymbol{u}, \boldsymbol{b}) + \left(\delta\boldsymbol{u}, \dfrac{1}{\rho}\hat{\boldsymbol{t}}\right)_{\Gamma_t} \\ \left(\delta\vartheta, \dot{\vartheta}\right) + \left(\boldsymbol{\nabla}\delta\vartheta, \dfrac{1}{\bar{c}}\bar{\boldsymbol{\kappa}}\boldsymbol{\nabla}\vartheta\right) + \left(\delta\vartheta, \dfrac{1}{\bar{c}}\boldsymbol{m} : \boldsymbol{\nabla}\boldsymbol{v}\right) = \left(\delta\vartheta, \dfrac{r}{c}\right) - \left(\delta\vartheta, \dfrac{\hat{q}}{c}\right)_{\Gamma_q} \end{cases} \tag{7}$$

The above weak form is only semi-discrete, meaning that it is discretized in the spatial domain but still continuous in the temporal domain. We use the Crank-Nicolson method as the time integrator to obtain an ODE system. We denote quantities at the middle of the time step as

$$(\cdot)^{(n+\frac{1}{2})} = \frac{(\cdot)^{(n)} + (\cdot)^{(n+1)}}{2}. \tag{8}$$

According to the Crank-Nicolson method, we have

$$\left(\delta\boldsymbol{v},\, \frac{\boldsymbol{u}^{(n+1)} - \boldsymbol{u}^{(n)}}{\Delta t}\right) = \left(\delta\boldsymbol{v},\, \boldsymbol{v}^{(n+\frac{1}{2})}\right), \tag{9}$$

$$\left(\delta\boldsymbol{u},\, \frac{\boldsymbol{v}^{(n+1)} - \boldsymbol{v}^{(n)}}{\Delta t}\right) + \left(\boldsymbol{\nabla}\delta\boldsymbol{u},\, \left[\frac{1}{\rho}\left(\mathbb{C} : \boldsymbol{\epsilon} - \vartheta\boldsymbol{m}\right)\right]^{(n+\frac{1}{2})}\right) = \left(\delta\boldsymbol{u},\, \boldsymbol{b}^{(n+\frac{1}{2})}\right) + \left(\delta\boldsymbol{u},\, \frac{1}{\rho}\hat{\boldsymbol{t}}^{(n+\frac{1}{2})}\right)_{\Gamma_t}, \tag{10}$$

and

$$\left(\delta\vartheta,\, \frac{\vartheta^{(n+1)} - \vartheta^{(n)}}{\Delta t}\right) + \left(\boldsymbol{\nabla}\delta\vartheta,\, \frac{1}{\bar{c}}\bar{\boldsymbol{\kappa}}\boldsymbol{\nabla}\vartheta^{(n+\frac{1}{2})}\right) + \left(\delta\vartheta,\, \frac{1}{\bar{c}}\boldsymbol{m} : \boldsymbol{\nabla}\boldsymbol{v}^{(n+\frac{1}{2})}\right) = \left(\delta\vartheta,\, \frac{r^{(n+\frac{1}{2})}}{c}\right) - \left(\delta\vartheta,\, \frac{\hat{q}^{(n+\frac{1}{2})}}{c}\right)_{\Gamma_q}. \tag{11}$$

Rearranging the above equations, we can obtain the fully discretized system as

$$\left(\delta\boldsymbol{v},\, \boldsymbol{u}^{(n+1)}\right) - \frac{\Delta t}{2}\left(\delta\boldsymbol{v},\, \boldsymbol{v}^{(n+1)}\right) = \left(\delta\boldsymbol{v},\, \boldsymbol{u}^{(n)}\right) + \frac{\Delta t}{2}\left(\delta\boldsymbol{v},\, \boldsymbol{v}^{(n)}\right), \tag{12}$$

$$\begin{aligned} &\left(\delta\boldsymbol{u},\, \boldsymbol{v}^{(n+1)}\right) + \frac{\Delta t}{2}\left(\boldsymbol{\nabla}\delta\boldsymbol{u},\, \frac{1}{\rho}\mathbb{C} : \boldsymbol{\epsilon}(\boldsymbol{u}^{(n+1)})\right) - \frac{\Delta t}{2}\left(\boldsymbol{\nabla}\delta\boldsymbol{u},\, \frac{1}{\rho}\vartheta^{(n+1)}\boldsymbol{m}\right) \\ &= \left(\delta\boldsymbol{u},\, \boldsymbol{v}^{(n)}\right) - \frac{\Delta t}{2}\left(\boldsymbol{\nabla}\delta\boldsymbol{u},\, \frac{1}{\rho}\mathbb{C} : \boldsymbol{\epsilon}(\boldsymbol{u}^{(n)})\right) + \frac{\Delta t}{2}\left(\boldsymbol{\nabla}\delta\boldsymbol{u},\, \frac{1}{\rho}\vartheta^{(n)}\boldsymbol{m}\right) + \Delta t\left(\delta\boldsymbol{u},\, \boldsymbol{b}^{(n+\frac{1}{2})}\right) + \Delta t\left(\delta\boldsymbol{u},\, \frac{1}{\rho}\hat{\boldsymbol{t}}^{(n+\frac{1}{2})}\right)_{\Gamma_t}, \end{aligned} \tag{13}$$

and

$$\begin{aligned} &\left(\delta\vartheta,\, \vartheta^{(n+1)}\right) + \frac{\Delta t}{2}\left(\boldsymbol{\nabla}\delta\vartheta,\, \frac{1}{\bar{c}}\bar{\boldsymbol{\kappa}}\boldsymbol{\nabla}\vartheta^{(n+1)}\right) + \frac{\Delta t}{2}\left(\delta\vartheta,\, \frac{1}{\bar{c}}\boldsymbol{m} : \boldsymbol{\nabla}\boldsymbol{v}^{(n+1)}\right) \\ &= \left(\delta\vartheta,\, \vartheta^{(n)}\right) - \frac{\Delta t}{2}\left(\boldsymbol{\nabla}\delta\vartheta,\, \frac{1}{\bar{c}}\bar{\boldsymbol{\kappa}}\boldsymbol{\nabla}\vartheta^{(n)}\right) - \frac{\Delta t}{2}\left(\delta\vartheta,\, \frac{1}{\bar{c}}\boldsymbol{m} : \boldsymbol{\nabla}\boldsymbol{v}^{(n)}\right) + \Delta t\left(\delta\vartheta,\, \frac{r^{(n+\frac{1}{2})}}{c}\right) - \Delta t\left(\delta\vartheta,\, \frac{\hat{q}^{(n+\frac{1}{2})}}{c}\right)_{\Gamma_q}. \end{aligned} \tag{14}$$

Recall that $\{\boldsymbol{v}, \boldsymbol{u}, \vartheta\}^{(n)}$ are known at the beginning of the time step, we can obtain the solutions at the end of the time step by solving the linear system

$$\begin{pmatrix} \mathbf{K}_{\boldsymbol{vv}} & \mathbf{K}_{\boldsymbol{vu}} & \mathbf{K}_{\boldsymbol{v}\vartheta} \\ \mathbf{K}_{\boldsymbol{uv}} & \mathbf{K}_{\boldsymbol{uu}} & \mathbf{K}_{\boldsymbol{u}\vartheta} \\ \mathbf{K}_{\vartheta\boldsymbol{v}} & \mathbf{K}_{\vartheta\boldsymbol{u}} & \mathbf{K}_{\vartheta\vartheta} \end{pmatrix} \begin{pmatrix} \boldsymbol{v} \\ \boldsymbol{u} \\ \vartheta \end{pmatrix}^{(n+1)} = \begin{pmatrix} \boldsymbol{F}_{\boldsymbol{v}} \\ \boldsymbol{F}_{\boldsymbol{u}} \\ \boldsymbol{F}_{\vartheta} \end{pmatrix}. \tag{15}$$

Let the subscripts i and j represent the finite element nodal numbers. Each entry of the above block matrices can be written as

$$\begin{aligned} &(\mathbf{K}_{\boldsymbol{vv}})_{ij} = -\frac{\Delta t}{2}\left(\delta\boldsymbol{v}_i,\, \delta\boldsymbol{v}_j\right), && (\mathbf{K}_{\boldsymbol{vu}})_{ij} = (\delta\boldsymbol{v}_i,\, \delta\boldsymbol{u}_j), && \mathbf{K}_{\boldsymbol{v}\vartheta} = \mathbf{0}, \\ &(\mathbf{K}_{\boldsymbol{uv}})_{ij} = (\delta\boldsymbol{u}_i,\, \delta\boldsymbol{v}_j), && (\mathbf{K}_{\boldsymbol{uu}})_{ij} = \frac{\Delta t}{2}\left(\boldsymbol{\nabla}\delta\boldsymbol{u}_i,\, \frac{1}{\rho}\mathbb{C} : \boldsymbol{\nabla}\delta\boldsymbol{u}_j\right), && (\mathbf{K}_{\boldsymbol{u}\vartheta})_{ij} = -\frac{\Delta t}{2}\left(\boldsymbol{\nabla}\delta\boldsymbol{u}_i,\, \frac{1}{\rho}\boldsymbol{m}\delta\vartheta_j\right), \\ &(\mathbf{K}_{\vartheta\boldsymbol{v}})_{ij} = \frac{\Delta t}{2}\left(\delta\vartheta_i,\, \frac{1}{\bar{c}}\boldsymbol{m} : \boldsymbol{\nabla}\delta\boldsymbol{v}_j\right), && \mathbf{K}_{\vartheta\boldsymbol{u}} = \mathbf{0}^{\mathrm{T}}, && (\mathbf{K}_{\vartheta\vartheta})_{ij} = (\delta\vartheta_i,\, \delta\vartheta_j) + \frac{\Delta t}{2}\left(\boldsymbol{\nabla}\delta\vartheta_i,\, \frac{1}{\bar{c}}\bar{\boldsymbol{\kappa}}\boldsymbol{\nabla}\vartheta_j\right), \end{aligned}$$

and

$$\begin{aligned} (\boldsymbol{F}_{\boldsymbol{v}})_i &= \left(\delta\boldsymbol{v}_i,\, \boldsymbol{u}^{(n)}\right) + \frac{\Delta t}{2}\left(\delta\boldsymbol{v}_i,\, \boldsymbol{v}^{(n)}\right), \\ (\boldsymbol{F}_{\boldsymbol{u}})_i &= \left(\delta\boldsymbol{u}_i,\, \boldsymbol{v}^{(n)}\right) - \frac{\Delta t}{2}\left(\boldsymbol{\nabla}\delta\boldsymbol{u}_i,\, \frac{1}{\rho}\mathbb{C} : \boldsymbol{\epsilon}(\boldsymbol{u}^{(n)})\right) + \frac{\Delta t}{2}\left(\boldsymbol{\nabla}\delta\boldsymbol{u}_i,\, \frac{1}{\rho}\vartheta^{(n)}\boldsymbol{m}\right) + \Delta t\left(\delta\boldsymbol{u}_i,\, \boldsymbol{b}^{(n+\frac{1}{2})}\right) + \Delta t\left(\delta\boldsymbol{u}_i,\, \frac{1}{\rho}\hat{\boldsymbol{t}}^{(n+\frac{1}{2})}\right)_{\Gamma_t}, \\ (\boldsymbol{F}_{\vartheta})_i &= \left(\delta\vartheta_i,\, \vartheta^{(n)}\right) - \frac{\Delta t}{2}\left(\boldsymbol{\nabla}\delta\vartheta_i,\, \frac{1}{\bar{c}}\bar{\boldsymbol{\kappa}}\boldsymbol{\nabla}\vartheta^{(n)}\right) - \frac{\Delta t}{2}\left(\delta\vartheta_i,\, \frac{1}{\bar{c}}\boldsymbol{m} : \boldsymbol{\nabla}\boldsymbol{v}^{(n)}\right) + \Delta t\left(\delta\vartheta_i,\, \frac{r^{(n+\frac{1}{2})}}{c}\right) - \Delta t\left(\delta\vartheta_i,\, \frac{\hat{q}^{(n+\frac{1}{2})}}{c}\right)_{\Gamma_q}. \end{aligned}$$

Notice that the above fully coupled linear system is unsymmetric.

2.3. Staggered approach

Instead of forming the fully coupled thermomechanical problem as a monolithic system, which typically results in an unsymmetric stiffness matrix and more expensive computational cost due to the size of the linear system, an alternative approach is to solve the thermomechanical problem following a staggered approach. That is, the fully coupled thermomechanical problem is split into two sub-problems, a mechanical sub-problem and a thermal sub-problem. Comparing with the monolithic approach, the staggered approach has several advantages. First, each sub-problem forms a smaller linear system that is typically symmetric. For problems with a large number of unknowns, in which iterative linear solvers would be more efficient than direct solvers, common iterative linear solvers such as the conjugate-gradient method can be easily applied. More importantly, unlike the monolithic approach in which a single type of time integration technique has to be applied to both fields (displacement and temperature in this case), the staggered approach is more flexible in the sense that different time integration techniques can be applied to individual unknown fields. Despite of the aforementioned advantages, if not designed carefully, the staggered approach may become only conditionally stable even enough the time integration technique applied to each field is unconditionally stable. In this section, we provide the finite element implementation details for two popular staggered schemes, the conditionally stable isothermal split and the unconditionally stable adiabatic split originally proposed by Armero and Simo [31]. For detailed numerical analysis about the stability of these two schemes, interested readers are referred to the work by Armero and Simo [31].

2.3.1. Isothermal split

According to the isothermal split, the semi-discrete weak form of the coupled thermomechanical system, as shown in Eq. (7), is partitioned into a mechanical phase and a thermal phase. In the mechanical phase of a typical time step $[t_n, t_{n+1}]$, the temperature is assumed to be constant (that is why it is called "isothermal") and the displacement field is updated, that is,

$$\{\boldsymbol{v}^{(n)}, \boldsymbol{u}^{(n)}, \vartheta^{(n)}\} \longrightarrow \{\boldsymbol{v}^{(n+1)}, \boldsymbol{u}^{(n+1)}, \vartheta^{(n)}\}.$$

Then, the temperature field is updated in the following thermal phase to conclude the current time step, that is,

$$\{\boldsymbol{v}^{(n+1)}, \boldsymbol{u}^{(n+1)}, \vartheta^{(n)}\} \longrightarrow \{\boldsymbol{v}^{(n+1)}, \boldsymbol{u}^{(n+1)}, \vartheta^{(n+1)}\}.$$

During the mechanical phase, we still adopt the Crank-Nicolson method for the time integration,

$$\left(\delta\boldsymbol{v},\, \boldsymbol{u}^{(n+1)}\right) - \frac{\Delta t}{2}\left(\delta\boldsymbol{v},\, \boldsymbol{v}^{(n+1)}\right) = \left(\delta\boldsymbol{v},\, \boldsymbol{u}^{(n)}\right) + \frac{\Delta t}{2}\left(\delta\boldsymbol{v},\, \boldsymbol{v}^{(n)}\right) \tag{16}$$

and

$$\begin{aligned}
&\left(\delta\boldsymbol{u},\, \boldsymbol{v}^{(n+1)}\right) + \frac{\Delta t}{2}\left(\boldsymbol{\nabla}\delta\boldsymbol{u},\, \frac{1}{\rho}\mathbb{C} : \boldsymbol{\epsilon}(\boldsymbol{u}^{(n+1)})\right) \\
&= \left(\delta\boldsymbol{u},\, \boldsymbol{v}^{(n)}\right) - \frac{\Delta t}{2}\left(\boldsymbol{\nabla}\delta\boldsymbol{u},\, \frac{1}{\rho}\mathbb{C} : \boldsymbol{\epsilon}(\boldsymbol{u}^{(n)})\right) + \Delta t\left(\boldsymbol{\nabla}\delta\boldsymbol{u},\, \frac{1}{\rho}\vartheta^{(n)}\boldsymbol{m}\right) + \Delta t\left(\delta\boldsymbol{u},\, \boldsymbol{b}^{(n+\frac{1}{2})}\right) + \Delta t\left(\delta\boldsymbol{u},\, \frac{1}{\rho}\hat{\boldsymbol{t}}^{(n+\frac{1}{2})}\right)_{\Gamma_t}.
\end{aligned} \tag{17}$$

Writing the above equations into a linear system, we have

$$\begin{pmatrix} \mathbf{K}_{\boldsymbol{vv}} & \mathbf{K}_{\boldsymbol{vu}} \\ \mathbf{K}_{\boldsymbol{uv}} & \mathbf{K}_{\boldsymbol{uu}} \end{pmatrix} \begin{pmatrix} \boldsymbol{v} \\ \boldsymbol{u} \end{pmatrix}^{(n+1)} = \begin{pmatrix} \boldsymbol{F}_{\boldsymbol{v}} \\ \boldsymbol{F}_{\boldsymbol{u}} \end{pmatrix} \tag{18}$$

where

$$\begin{aligned}
&(\mathbf{K}_{\boldsymbol{vv}})_{ij} = -\frac{\Delta t}{2}\left(\delta\boldsymbol{v}_i,\, \delta\boldsymbol{v}_j\right), && (\mathbf{K}_{\boldsymbol{vu}})_{ij} = \left(\delta\boldsymbol{v}_i,\, \delta\boldsymbol{u}_j\right), \\
&(\mathbf{K}_{\boldsymbol{uv}})_{ij} = \left(\delta\boldsymbol{u}_i,\, \delta\boldsymbol{v}_j\right), && (\mathbf{K}_{\boldsymbol{uu}})_{ij} = \frac{\Delta t}{2}\left(\boldsymbol{\nabla}\delta\boldsymbol{u}_i,\, \frac{1}{\rho}\mathbb{C} : \boldsymbol{\nabla}(\delta\boldsymbol{u}_j)\right),
\end{aligned}$$

and

$$\begin{aligned}
(\boldsymbol{F}_{\boldsymbol{v}})_i &= \left(\delta\boldsymbol{v}_i,\, \boldsymbol{u}^{(n)}\right) + \frac{\Delta t}{2}\left(\delta\boldsymbol{v}_i,\, \boldsymbol{v}^{(n)}\right), \\
(\boldsymbol{F}_{\boldsymbol{u}})_i &= \left(\delta\boldsymbol{u}_i,\, \boldsymbol{v}^{(n)}\right) - \frac{\Delta t}{2}\left(\boldsymbol{\nabla}\delta\boldsymbol{u}_i,\, \frac{1}{\rho}\mathbb{C} : \boldsymbol{\epsilon}(\boldsymbol{u}^{(n)})\right) + \Delta t\left(\boldsymbol{\nabla}\delta\boldsymbol{u}_i,\, \frac{1}{\rho}\vartheta^{(n)}\boldsymbol{m}\right) + \Delta t\left(\delta\boldsymbol{u}_i,\, \boldsymbol{b}^{(n+\frac{1}{2})}\right) + \Delta t\left(\delta\boldsymbol{u}_i,\, \frac{1}{\rho}\hat{\boldsymbol{t}}^{(n+\frac{1}{2})}\right)_{\Gamma_t}.
\end{aligned}$$

By solving the above linear system, which is symmetric, we can obtain the new deformation field and then update the temperature field during the thermal phase. Recall that $\boldsymbol{v}^{(n+1)}$ and $\boldsymbol{u}^{(n+1)}$ are already solved from the mechanical phase, we only need to solve the temperature field.

As aforementioned, the advantage of the staggered approach is that different time integration techniques can be applied to update each unknown fields. If the Crank-Nicolson method is adopted for the thermal sub-problem, we have the fully discrete system as

$$\begin{aligned}
&\left(\delta\vartheta,\, \vartheta^{(n+1)}\right) + \frac{\Delta t}{2}\left(\boldsymbol{\nabla}\delta\vartheta,\, \frac{1}{\bar{c}}\bar{\boldsymbol{\kappa}}\boldsymbol{\nabla}\vartheta^{(n+1)}\right) \\
&= \left(\delta\vartheta,\, \vartheta^{(n)}\right) - \frac{\Delta t}{2}\left(\boldsymbol{\nabla}\delta\vartheta,\, \frac{1}{\bar{c}}\bar{\boldsymbol{k}}\boldsymbol{\nabla}\vartheta^{(n)}\right) - \Delta t\left(\delta\vartheta,\, \frac{1}{\bar{c}}\boldsymbol{m} : \boldsymbol{\nabla}\boldsymbol{v}^{(n+1)}\right) + \Delta t\left(\delta\vartheta,\, \frac{r^{(n+\frac{1}{2})}}{c}\right) - \Delta t\left(\delta\vartheta,\, \frac{\hat{q}^{(n+\frac{1}{2})}}{c}\right)_{\Gamma_q}.
\end{aligned} \tag{19}$$

We can write the above equation into the following linear system

$$\mathbf{K}_{\vartheta\vartheta}\, \vartheta^{(n+1)} = \boldsymbol{F}_{\vartheta}, \tag{20}$$

where

$$(\mathbf{K}_{\vartheta\vartheta})_{ij} = \left(\delta\vartheta_i,\, \delta\vartheta_j\right) + \frac{\Delta t}{2}\left(\boldsymbol{\nabla}\delta\vartheta_i,\, \frac{1}{\bar{c}}\bar{\boldsymbol{\kappa}}\boldsymbol{\nabla}\delta\vartheta_j\right)$$

and

$$(\boldsymbol{F}_\vartheta)_i = \left(\delta\vartheta_i,\, \vartheta^{(n)}\right) - \frac{\Delta t}{2}\left(\boldsymbol{\nabla}\delta\vartheta_i,\, \frac{1}{\bar{c}}\bar{\boldsymbol{k}}\boldsymbol{\nabla}\vartheta^{(n)}\right) - \Delta t\left(\delta\vartheta_i,\, \frac{1}{\bar{c}}\boldsymbol{m} : \boldsymbol{\nabla}\boldsymbol{v}^{(n+1)}\right) + \Delta t\left(\delta\vartheta_i,\, \frac{r^{(n+\frac{1}{2})}}{c}\right) - \Delta t\left(\delta\vartheta_i,\, \frac{\hat{q}^{(n+\frac{1}{2})}}{c}\right)_{\Gamma_q}.$$

On the other hand, if the backward Euler method is applied to the thermal phase, we obtain the following fully discrete system

$$\begin{aligned}&\left(\delta\vartheta,\, \vartheta^{(n+1)}\right) + \Delta t\left(\boldsymbol{\nabla}\delta\vartheta,\, \frac{1}{\bar{c}}\bar{\boldsymbol{\kappa}}\boldsymbol{\nabla}\vartheta^{(n+1)}\right)\\ &= \left(\delta\vartheta,\, \vartheta^{(n)}\right) - \Delta t\left(\delta\vartheta,\, \frac{1}{\bar{c}}\boldsymbol{m} : \boldsymbol{\nabla}\boldsymbol{v}^{(n+1)}\right) + \Delta t\left(\delta\vartheta,\, \frac{r^{(n+1)}}{c}\right) - \Delta t\left(\delta\vartheta,\, \frac{\hat{q}^{(n+1)}}{c}\right)_{\Gamma_q}.\end{aligned} \tag{21}$$

The matrix and the right-hand side in Eq. (20) become

$$(\mathbf{K}_{\vartheta\vartheta})_{ij} = \left(\delta\vartheta_i,\, \delta\vartheta_j\right) + \Delta t\left(\boldsymbol{\nabla}\delta\vartheta_i,\, \frac{1}{\bar{c}}\bar{\boldsymbol{\kappa}}\boldsymbol{\nabla}\delta\vartheta_j\right)$$

and

$$(\boldsymbol{F}_\vartheta)_i = \left(\delta\vartheta_i,\, \vartheta^{(n)}\right) - \Delta t\left(\delta\vartheta_i,\, \frac{1}{\bar{c}}\boldsymbol{m} : \boldsymbol{\nabla}\boldsymbol{v}^{(n+1)}\right) + \Delta t\left(\delta\vartheta_i,\, \frac{r^{(n+\frac{1}{2})}}{c}\right) - \Delta t\left(\delta\vartheta_i,\, \frac{\hat{q}^{(n+\frac{1}{2})}}{c}\right)_{\Gamma_q}.$$

Even though both the Crank-Nicolson method and the backward Euler method are unconditionally stable, the staggered approach based on the isothermal split (constant temperature) is only conditionally stable. This is the motivation for designing a better staggered approach, for instance, the adiabatic split (constant entropy), that is able to maintain the unconditional stability.

2.3.2. Adiabatic split

Similar to the isothermal split, the staggered approach based on the adiabatic split also partitions the fully coupled thermomechanical problem into the mechanical phase sub-problem and the thermal phase sub-problem. Unlike the isothermal split in which the temperature is kept constant, the adiabatic split maintains a constant entropy between the mechanical phase and the thermal phase [31]. Assume that $\boldsymbol{u}_t$ and ϑ_t represent some intermediate solutions, since the entropy is kept constant,

$$\begin{aligned}\eta^{(n)} = \eta_t \quad &\Rightarrow \quad \boldsymbol{m} : \boldsymbol{\epsilon}(\boldsymbol{u}^{(n)}) + \bar{c}\vartheta^{(n)} = \boldsymbol{m} : \boldsymbol{\epsilon}(\boldsymbol{u}_t) + \bar{c}\vartheta_t\\ &\Rightarrow \quad \vartheta_t = \vartheta^{(n)} - \frac{1}{\bar{c}}\boldsymbol{m} : \left[\boldsymbol{\epsilon}(\boldsymbol{u}_t) - \boldsymbol{\epsilon}(\boldsymbol{u}^{(n)})\right].\end{aligned} \tag{22}$$

During the mechanical phase, the deformation is updated as

$$\{\boldsymbol{v}^{(n)}, \boldsymbol{u}^{(n)}, \vartheta^{(n)}\} \longrightarrow \{\boldsymbol{v}^{(n+1)}, \boldsymbol{u}^{(n+1)}, \vartheta_t\},$$

where $\boldsymbol{v}^{(n+1)} = \boldsymbol{v}_t$ and $\boldsymbol{u}^{(n+1)} = \boldsymbol{u}_t$ such that the entropy is unchanged. During the thermal phase, the temperature field is updated as

$$\{\boldsymbol{v}^{(n+1)}, \boldsymbol{u}^{(n+1)}, \vartheta_t\} \longrightarrow \{\boldsymbol{v}^{(n+1)}, \boldsymbol{u}^{(n+1)}, \vartheta^{(n+1)}\}.$$

Plug in the expression of the intermediate temperature shown in Eq. (22) into the semi-discrete weak form Eq. (7) and apply the Crank-Nicolson method, we have

$$\left(\delta\boldsymbol{v},\, \boldsymbol{u}^{(n+1)}\right) - \frac{\Delta t}{2}\left(\delta\boldsymbol{v},\, \boldsymbol{v}^{(n+1)}\right) = \left(\delta\boldsymbol{v},\, \boldsymbol{u}^{(n)}\right) + \frac{\Delta t}{2}\left(\delta\boldsymbol{v},\, \boldsymbol{v}^{(n)}\right) \tag{23}$$

and

$$\begin{aligned}&\left(\delta\boldsymbol{u},\, \boldsymbol{v}^{(n+1)}\right) + \frac{\Delta t}{2}\left(\boldsymbol{\nabla}\delta\boldsymbol{u},\, \frac{1}{\rho}\mathbb{C}^{\mathrm{ad}} : \boldsymbol{\epsilon}(\boldsymbol{u}^{(n+1)})\right)\\ &= \left(\delta\boldsymbol{u},\, \boldsymbol{v}^{(n)}\right) - \frac{\Delta t}{2}\left(\boldsymbol{\nabla}\delta\boldsymbol{u},\, \frac{1}{\rho}\mathbb{C}^{\mathrm{ad}} : \boldsymbol{\epsilon}(\boldsymbol{u}^{(n)})\right) + \Delta t\left(\delta\boldsymbol{u},\, \boldsymbol{b}^{(n+\frac{1}{2})}\right)\\ &\quad + \Delta t\left(\delta\boldsymbol{u},\, \frac{1}{\rho}\hat{\boldsymbol{t}}^{(n+\frac{1}{2})}\right)_{\Gamma_t} + \Delta t\left(\boldsymbol{\nabla}\delta\boldsymbol{u},\, \frac{1}{\rho}\boldsymbol{m}\left[\frac{\boldsymbol{m} : \boldsymbol{\epsilon}(\boldsymbol{u}^{(n)})}{\bar{c}} + \vartheta^{(n)}\right]\right),\end{aligned} \tag{24}$$

where the modified material stiffness tensor is

$$\mathbb{C}^{\mathrm{ad}} = \mathbb{C} + \frac{1}{\bar{c}}\boldsymbol{m} \otimes \boldsymbol{m}.$$

Writing the above equations as a linear system, we have

$$\begin{pmatrix} \mathbf{K}_{\boldsymbol{vv}} & \mathbf{K}_{\boldsymbol{vu}} \\ \mathbf{K}_{\boldsymbol{uv}} & \mathbf{K}_{\boldsymbol{uu}} \end{pmatrix} \begin{pmatrix} \boldsymbol{v} \\ \boldsymbol{u} \end{pmatrix}^{(n+1)} = \begin{pmatrix} \boldsymbol{F}_{\boldsymbol{v}} \\ \boldsymbol{F}_{\boldsymbol{u}} \end{pmatrix}, \tag{25}$$

where

$$(\mathbf{K}_{\boldsymbol{vv}})_{ij} = -\frac{\Delta t}{2}\left(\delta \boldsymbol{v}_i, \delta \boldsymbol{v}_j\right), \qquad (\mathbf{K}_{\boldsymbol{vu}})_{ij} = \left(\delta \boldsymbol{v}_i, \delta \boldsymbol{u}_j\right),$$
$$(\mathbf{K}_{\boldsymbol{uv}})_{ij} = \left(\delta \boldsymbol{u}_i, \delta \boldsymbol{v}_j\right), \qquad (\mathbf{K}_{\boldsymbol{uu}})_{ij} = \frac{\Delta t}{2}\left(\boldsymbol{\nabla}\delta \boldsymbol{u}_i, \frac{1}{\rho}\mathbb{C}^{\mathrm{ad}} : \boldsymbol{\nabla}\delta \boldsymbol{u}_j\right),$$

and

$$\begin{aligned} (\boldsymbol{F}_{\boldsymbol{v}})_i &= \left(\delta \boldsymbol{v}_i, \boldsymbol{u}^{(n)}\right) + \frac{\Delta t}{2}\left(\delta \boldsymbol{v}_i, \boldsymbol{v}^{(n)}\right), \\ (\boldsymbol{F}_{\boldsymbol{u}})_i &= \left(\delta \boldsymbol{u}_i, \boldsymbol{v}^{(n)}\right) - \frac{\Delta t}{2}\left(\boldsymbol{\nabla}\delta \boldsymbol{u}_i, \frac{1}{\rho}\mathbb{C}^{\mathrm{ad}} : \boldsymbol{\epsilon}(\boldsymbol{u}^{(n)})\right) + \Delta t\left(\delta \boldsymbol{u}_i, \boldsymbol{b}^{(n+\frac{1}{2})}\right) \\ &\quad + \Delta t\left(\delta \boldsymbol{u}_i, \frac{1}{\rho}\hat{\boldsymbol{t}}^{(n+\frac{1}{2})}\right)_{\Gamma_t} + \Delta t\left(\boldsymbol{\nabla}\delta \boldsymbol{u}_i, \frac{1}{\rho}\boldsymbol{m}\left[\frac{\boldsymbol{m} : \boldsymbol{\epsilon}(\boldsymbol{u}^{(n)})}{\bar{c}} + \vartheta^{(n)}\right]\right). \end{aligned}$$

For the thermal phase in the adiabatic split, if the Crank-Nicolson method is applied, we have

$$\begin{aligned} &\left(\delta\vartheta, \vartheta^{(n+1)}\right) + \frac{\Delta t}{2}\left(\boldsymbol{\nabla}\delta\vartheta, \frac{1}{\bar{c}}\bar{\boldsymbol{\kappa}}\boldsymbol{\nabla}\vartheta^{(n+1)}\right) \\ &= \left(\delta\vartheta, \vartheta^{(n)}\right) - \frac{\Delta t}{2}\left(\boldsymbol{\nabla}\delta\vartheta, \frac{1}{\bar{c}}\bar{\boldsymbol{k}}\boldsymbol{\nabla}\vartheta^{(n)}\right) - \left(\delta\vartheta, \frac{1}{\bar{c}}\boldsymbol{m} : \boldsymbol{\epsilon}(\boldsymbol{u}^{(n+1)})\right) \\ &\quad + \left(\delta\vartheta, \frac{1}{\bar{c}}\boldsymbol{m} : \boldsymbol{\epsilon}(\boldsymbol{u}^{(n)})\right) + \Delta t\left(\delta\vartheta, \frac{r^{(n+\frac{1}{2})}}{c}\right) - \Delta t\left(\delta\vartheta, \frac{\hat{q}^{(n+\frac{1}{2})}}{c}\right)_{\Gamma_q}. \end{aligned} \tag{26}$$

We can write the above equation into a linear system

$$\mathbf{K}_{\vartheta\vartheta}\,\vartheta^{(n+1)} = \boldsymbol{F}_{\vartheta}, \tag{27}$$

where

$$(\mathbf{K}_{\vartheta\vartheta})_{ij} = \left(\delta\vartheta_i, \delta\vartheta_j\right) + \frac{\Delta t}{2}\left(\boldsymbol{\nabla}\delta\vartheta_i, \frac{1}{\bar{c}}\bar{\boldsymbol{\kappa}}\boldsymbol{\nabla}\delta\vartheta_j\right)$$

and

$$\begin{aligned} (\boldsymbol{F}_{\vartheta})_i &= \left(\delta\vartheta_i, \vartheta^{(n)}\right) - \frac{\Delta t}{2}\left(\boldsymbol{\nabla}\delta\vartheta_i, \frac{1}{\bar{c}}\bar{\boldsymbol{k}}\boldsymbol{\nabla}\vartheta^{(n)}\right) - \left(\delta\vartheta_i, \frac{1}{\bar{c}}\boldsymbol{m} : \boldsymbol{\epsilon}(\boldsymbol{u}^{(n+1)})\right) \\ &\quad + \left(\delta\vartheta_i, \frac{1}{\bar{c}}\boldsymbol{m} : \boldsymbol{\epsilon}(\boldsymbol{u}^{(n)})\right) + \Delta t\left(\delta\vartheta_i, \frac{r^{(n+\frac{1}{2})}}{c}\right) - \Delta t\left(\delta\vartheta_i, \frac{\hat{q}^{(n+\frac{1}{2})}}{c}\right)_{\Gamma_q}. \end{aligned}$$

If the backward Euler method is applied to the thermal phase in the adiabatic split, we have

$$\begin{aligned} &\left(\delta\vartheta, \vartheta^{(n+1)}\right) + \Delta t\left(\boldsymbol{\nabla}\delta\vartheta, \frac{1}{\bar{c}}\bar{\boldsymbol{\kappa}}\boldsymbol{\nabla}\vartheta^{(n+1)}\right) \\ &= \left(\delta\vartheta, \vartheta^{(n)}\right) + \left(\delta\vartheta, \frac{1}{\bar{c}}\boldsymbol{m} : \boldsymbol{\epsilon}(\boldsymbol{u}^{(n)})\right) - \left(\delta\vartheta, \frac{1}{\bar{c}}\boldsymbol{m} : \boldsymbol{\epsilon}(\boldsymbol{u}^{(n+1)})\right) + \Delta t\left(\delta\vartheta, \frac{r^{(n+1)}}{c}\right) - \Delta t\left(\delta\vartheta, \frac{\hat{q}^{(n+1)}}{c}\right)_{\Gamma_q}. \end{aligned} \tag{28}$$

The matrix and the right-hand side in Eq. (27) become

$$(\mathbf{K}_{\vartheta\vartheta})_{ij} = \left(\delta\vartheta_i, \delta\vartheta_j\right) + \Delta t\left(\boldsymbol{\nabla}\delta\vartheta_i, \frac{1}{\bar{c}}\bar{\boldsymbol{\kappa}}\boldsymbol{\nabla}\delta\vartheta_j\right)$$

and

$$(\boldsymbol{F}_{\vartheta})_i = \left(\delta\vartheta_i, \vartheta^{(n)}\right) + \left(\delta\vartheta_i, \frac{1}{\bar{c}}\boldsymbol{m} : \boldsymbol{\epsilon}(\boldsymbol{u}^{(n)})\right) - \left(\delta\vartheta_i, \frac{1}{\bar{c}}\boldsymbol{m} : \boldsymbol{\epsilon}(\boldsymbol{u}^{(n+1)})\right) + \Delta t\left(\delta\vartheta_i, \frac{r^{(n+1)}}{c}\right) - \Delta t\left(\delta\vartheta_i, \frac{\hat{q}^{(n+1)}}{c}\right)_{\Gamma_q}.$$

As illustrated in the numerical example section, the choice of the time integration technique for the thermal phase would have impacts on the numerical results when stiff boundary conditions are applied.

2.4. Numerical implementation

To facilitate the numerical implementation, we provide the pseudo code for the monolithic approach and the two staggered approaches based on the isothermal split and the adiabatic split, respectively. Algorithm 1 provides the pseudo code for the monolithic approach. Even though this algorithm is relatively straightforward, inside each time step, we still need to assemble and solve a fully coupled linear system according to Eq. (15). As shown in the subsequent numerical examples, solving the fully coupled unsymmetric linear system is significantly more expensive.

Algorithm 1 Monolithic approach for the thermomechanically coupled problem.

```
Set the solution vector $\{\boldsymbol{v},\boldsymbol{u},\vartheta\} = \{\boldsymbol{v},\boldsymbol{u},\vartheta\}^{(0)}$.    ▷ Initial conditions
for $n = 0, \dots, N$ do    ▷ Loop over time steps
    Set $\{\boldsymbol{v},\boldsymbol{u},\vartheta\} = \{\boldsymbol{v},\boldsymbol{u},\vartheta\}^{(n)}$.    ▷ Solution at the beginning of the time step is known
    Assemble the block matrix $\begin{pmatrix} \mathbf{K}_{vv} & \mathbf{K}_{vu} & \mathbf{K}_{v\vartheta} \\ \mathbf{K}_{uv} & \mathbf{K}_{uu} & \mathbf{K}_{u\vartheta} \\ \mathbf{K}_{\vartheta v} & \mathbf{K}_{\vartheta u} & \mathbf{K}_{\vartheta\vartheta} \end{pmatrix}$ according to Eq. (15).
    Assemble the right-hand side $\begin{pmatrix} \boldsymbol{F}_v \\ \boldsymbol{F}_u \\ \boldsymbol{F}_\vartheta \end{pmatrix}$ based on the old solution $\{\boldsymbol{v},\boldsymbol{u},\vartheta\}^{(n)}$ according to Eq. (15).
    Solve the fully coupled linear system $\begin{pmatrix} \mathbf{K}_{vv} & \mathbf{K}_{vu} & \mathbf{K}_{v\vartheta} \\ \mathbf{K}_{uv} & \mathbf{K}_{uu} & \mathbf{K}_{u\vartheta} \\ \mathbf{K}_{\vartheta v} & \mathbf{K}_{\vartheta u} & \mathbf{K}_{\vartheta\vartheta} \end{pmatrix} \begin{pmatrix} \boldsymbol{v} \\ \boldsymbol{u} \\ \vartheta \end{pmatrix}^{(n+1)} = \begin{pmatrix} \boldsymbol{F}_v \\ \boldsymbol{F}_u \\ \boldsymbol{F}_\vartheta \end{pmatrix}$.
    Update the solution $\{\boldsymbol{v},\boldsymbol{u},\vartheta\}^{(n)} \longrightarrow \{\boldsymbol{v},\boldsymbol{u},\vartheta\}^{(n+1)}$ at the end of the current time step.
end for
```

Algorithm 2 Staggered approach based on the isothermal split for the thermomechanically coupled problem.

```
Set the solution vector $\{\boldsymbol{v},\boldsymbol{u},\vartheta\} = \{\boldsymbol{v},\boldsymbol{u},\vartheta\}^{(0)}$.    ▷ Initial conditions
for $n = 0, \dots, N$ do    ▷ Loop over time steps
    Set $\{\boldsymbol{v},\boldsymbol{u},\vartheta\} = \{\boldsymbol{v},\boldsymbol{u},\vartheta\}^{(n)}$.    ▷ Solution at the beginning of the time step is known
    Assemble the block matrix $\begin{pmatrix} \mathbf{K}_{vv} & \mathbf{K}_{vu} \\ \mathbf{K}_{uv} & \mathbf{K}_{uu} \end{pmatrix}$ according to Eq. (18).
    Assemble the right-hand side $\begin{pmatrix} \boldsymbol{F}_v \\ \boldsymbol{F}_u \end{pmatrix}$ based on the old solution $\{\boldsymbol{v},\boldsymbol{u},\vartheta\}^{(n)}$ according to Eq. (18).
    Solve the linear system (mechanical phase) $\begin{pmatrix} \mathbf{K}_{vv} & \mathbf{K}_{vu} \\ \mathbf{K}_{uv} & \mathbf{K}_{uu} \end{pmatrix} \begin{pmatrix} \boldsymbol{v} \\ \boldsymbol{u} \end{pmatrix}^{(n+1)} = \begin{pmatrix} \boldsymbol{F}_v \\ \boldsymbol{F}_u \end{pmatrix}$.
    Update the solution $\{\boldsymbol{v}^{(n)},\boldsymbol{u}^{(n)},\vartheta^{(n)}\} \longrightarrow \{\boldsymbol{v}^{(n+1)},\boldsymbol{u}^{(n+1)},\vartheta^{(n)}\}$.    ▷ Temperature is kept constant.
    Assemble the matrix $\mathbf{K}_{\vartheta\vartheta}$ and the right-hand side $\boldsymbol{F}_\vartheta$ based on $\{\boldsymbol{v}^{(n+1)},\boldsymbol{u}^{(n+1)},\vartheta^{(n)}\}$.
    Solve the linear system (thermal phase) $\mathbf{K}_{\vartheta\vartheta}\,\vartheta^{(n+1)} = \boldsymbol{F}_\vartheta$.
    Update the solution $\{\boldsymbol{v}^{(n+1)},\boldsymbol{u}^{(n+1)},\vartheta^{(n)}\} \longrightarrow \{\boldsymbol{v}^{(n+1)},\boldsymbol{u}^{(n+1)},\vartheta^{(n+1)}\}$ at the end of the current time step.
end for
```

Algorithms 2 and 3 provide the pseudo code for the staggered approaches based on the isothermal split and the adiabatic split, respectively. Comparing with the monolithic approach, we can see that in the staggered approaches, we divide the thermomechanically coupled problem into the mechanical sub-problem and the thermal sub-problem. For each sub-problem, a symmetric linear system is formed and solved for the corresponding unknowns. The key difference between the two staggered approaches is that, in the isothermal split, the temperature is kept constant in the intermediate state, while in the adiabatic split, the entropy is kept constant in the intermediate state.

Algorithm 3 Staggered approach based on the adiabatic split for the thermomechanically coupled problem.

```
Set the solution vector $\{\boldsymbol{v},\boldsymbol{u},\vartheta\} = \{\boldsymbol{v},\boldsymbol{u},\vartheta\}^{(0)}$.    ▷ Initial conditions
for $n = 0, \dots, N$ do    ▷ Loop over time steps
    Set $\{\boldsymbol{v},\boldsymbol{u},\vartheta\} = \{\boldsymbol{v},\boldsymbol{u},\vartheta\}^{(n)}$.    ▷ Solution at the beginning of the time step is known
    Form the modified material stiffness tensor $\mathbb{C}^{\mathrm{ad}} = \mathbb{C} + \frac{1}{\tilde{c}}\boldsymbol{m} \otimes \boldsymbol{m}$.
    Assemble the block matrix $\begin{pmatrix} \mathbf{K}_{vv} & \mathbf{K}_{vu} \\ \mathbf{K}_{uv} & \mathbf{K}_{uu} \end{pmatrix}$ based on $\mathbb{C}^{\mathrm{ad}}$ according to Eq. (25).
    Assemble the right-hand side $\begin{pmatrix} \boldsymbol{F}_v \\ \boldsymbol{F}_u \end{pmatrix}$ based on the old solution $\{\boldsymbol{v},\boldsymbol{u},\vartheta\}^{(n)}$ and $\mathbb{C}^{\mathrm{ad}}$ according to Eq. (25).
    Solve the linear system (mechanical phase) $\begin{pmatrix} \mathbf{K}_{vv} & \mathbf{K}_{vu} \\ \mathbf{K}_{uv} & \mathbf{K}_{uu} \end{pmatrix} \begin{pmatrix} \boldsymbol{v} \\ \boldsymbol{u} \end{pmatrix}^{(n+1)} = \begin{pmatrix} \boldsymbol{F}_v \\ \boldsymbol{F}_u \end{pmatrix}$.
    Update the solution $\{\boldsymbol{v}^{(n)},\boldsymbol{u}^{(n)},\vartheta^{(n)}\} \longrightarrow \{\boldsymbol{v}^{(n+1)},\boldsymbol{u}^{(n+1)},\vartheta_t\}$.    ▷ Entropy is kept constant.
    Assemble the matrix $\mathbf{K}_{\vartheta\vartheta}$ and the right-hand side $\boldsymbol{F}_\vartheta$ based on $\{\boldsymbol{v}^{(n+1)},\boldsymbol{u}^{(n+1)},\vartheta_t\}$.
    Solve the linear system (thermal phase) $\mathbf{K}_{\vartheta\vartheta}\,\vartheta^{(n+1)} = \boldsymbol{F}_\vartheta$.
    Update the solution $\{\boldsymbol{v}^{(n+1)},\boldsymbol{u}^{(n+1)},\vartheta_t\} \longrightarrow \{\boldsymbol{v}^{(n+1)},\boldsymbol{u}^{(n+1)},\vartheta^{(n+1)}\}$ at the end of the current time step.
end for
```

3. Numerical verification

In this section, we provide a dimensionless numerical example to compare the stability properties of various numerical algorithms, including the monolithic approach that is used as the reference solution, as well as the staggered approaches based on the isothermal

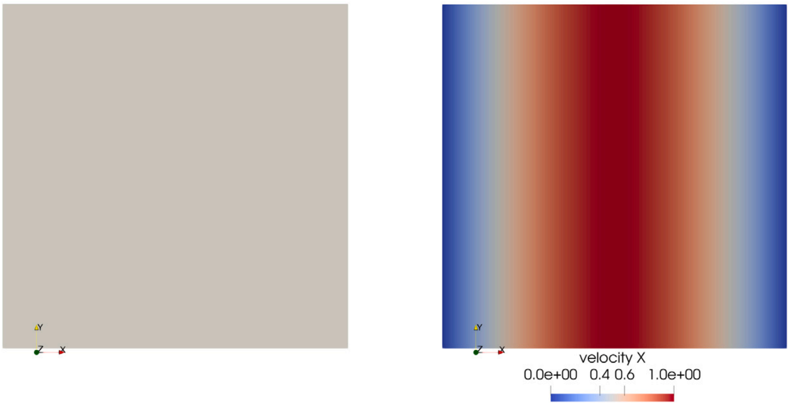

(a) Computational domain (b) Initial velocity v_x

Fig. 1. (a) The 100×100 two-dimensional computational domain to numerically verify the stability of different algorithms for the thermomechanically coupled problem. (b) The initial conditions are set up such that only the initial velocity v_x is non-zero.

split and the adiabatic split, respectively. The computational domain of a square with edge length $L = 100$ is shown in Fig. 1(a). The boundary conditions are prescribed such that the velocity, the displacement, and the temperature fields at the four edges of the computational domain are all zeros (homogeneous),

$$\boldsymbol{v}(0, y, t) = \boldsymbol{v}(L, y, t) = \boldsymbol{v}(x, 0, t) = \boldsymbol{v}(x, L, t) = \mathbf{0},$$

$$\boldsymbol{u}(0, y, t) = \boldsymbol{u}(L, y, t) = \boldsymbol{u}(x, 0, t) = \boldsymbol{u}(x, L, t) = \mathbf{0},$$

$$\vartheta(0, y, t) = \vartheta(L, y, t) = \vartheta(x, 0, t) = \vartheta(x, L, t) = 0.$$

The initial conditions are set up such that

$$v_x(x, y, 0) = \sin \frac{\pi x}{L}, \quad v_y(x, y, 0) = 0, \quad \boldsymbol{u}(x, y, 0) = \mathbf{0}, \quad \vartheta(x, y, 0) = 0.$$

The initial velocity in the x-direction v_x, which follows a sinusoidal distribution, is shown in Fig. 1(b). The computational domain is discretized by a structured finite element mesh with the mesh size $h = 1.0$ and a finite element space of bilinear shape functions $\mathrm{Q}_1 \times \mathrm{Q}_1 \times \mathrm{Q}_1$ for the velocity, the displacement, and the temperature fields, respectively. The material constitutive model shown in Eq. (2) is adopted. For the material mechanical behavior, we adopt the linear elasticity with the material tangent stiffness defined as

$$(\mathbb{C})_{ijkl} = \lambda \delta_{ij} \delta_{kl} + \mu(\delta_{ik} \delta_{jl} + \delta_{il} \delta_{jk})$$

with the Lamé parameters $\lambda = 0.5$ and $\mu = 0.25$. The thermal conductivity tensor is assumed to be isotropic, that is,

$$(\boldsymbol{\kappa})_{ij} = \kappa\, \delta_{ij},$$

where the thermal conductivity coefficient is $\kappa = 1.0$. The other parameters include the density $\rho = 1.0$, the specific heat $c_s = 1.0$, the reference temperature $\Theta_{\text{ref}} = 1.0$, and the thermal expansion coefficient $\beta = 0.5$ that measures the strength of the coupling between the material mechanical and thermal behaviors.

In order to demonstrate the stability of various numerical techniques described in Section 2, we apply two different time step sizes $\Delta t = 0.5$ and $\Delta t = 1.0$ to model the dynamic responses of the aforementioned initial boundary value problem (IBVP) during a time interval [0, 300]. Figs. 2 and 3 show the spatial distributions of the displacement field u_x, u_y, and the relative temperature field ϑ with time step size $\Delta t = 0.5$ at time $t = 100$ and $t = 200$. We can see the numerical results from the staggered approaches based on the isothermal split and the adiabatic split both match the monolithic results, which are considered as the reference solutions. On the other hand, when the time step size Δt is increased to 1.0, from Figs. 4 and 5 we can see that the numerical results of the adiabatic split still match the counterparts of the monolithic approach at both $t = 100$ and $t = 200$. However, the relative temperature field obtained from the isothermal split starts to become unstable at $t = 100$. As the time advances, for example, at $t = 200$, the instability becomes obvious across the whole computational domain for all the numerical results based on the isothermal split.

The conditional stability of the staggered approach based on the isothermal split is also manifested locally. Fig. 6 demonstrates the time history of the displacement field u_x, u_y, and the relative temperature field ϑ at the small time step size $\Delta t = 0.5$. The numerical results obtained from all the three approaches are similar. However, when the time step size Δt is doubled, that is, $\Delta t = 1.0$, the numerical results from the adiabatic split are still stable and match the monolithic results as shown in Fig. 7. However, the staggered approach based on the isothermal split becomes unstable at around $t = 150$.

From this example, we can see that even though individual time integration techniques for the mechanical phase and the thermal phase in a thermomechanically coupled problem, such as the Crank-Nicolson method and the backward Euler method, are unconditionally stable, the staggered approach based on the isothermal split becomes only conditionally stable. On the other hand, the

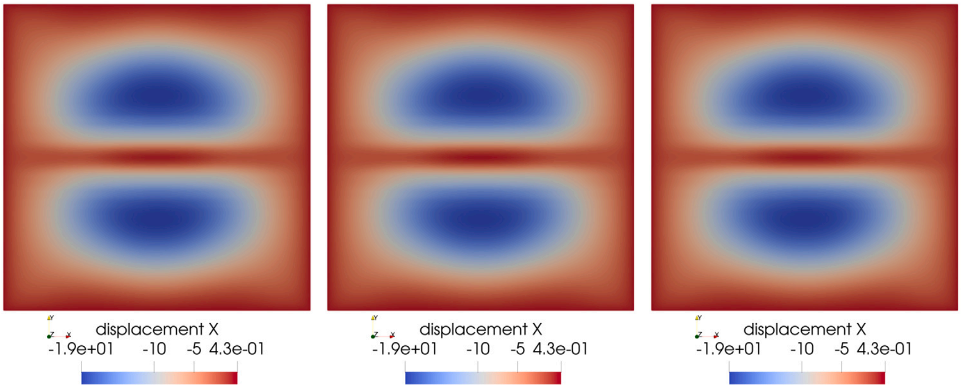

(a) u_x (monolithic) (b) u_x (isothermal split) (c) u_x (adiabatic split)

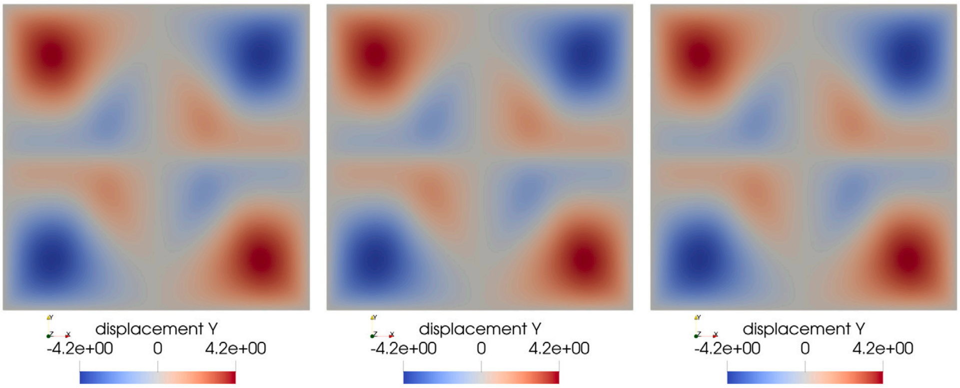

(d) u_y (monolithic) (e) u_y (isothermal split) (f) u_y (adiabatic split)

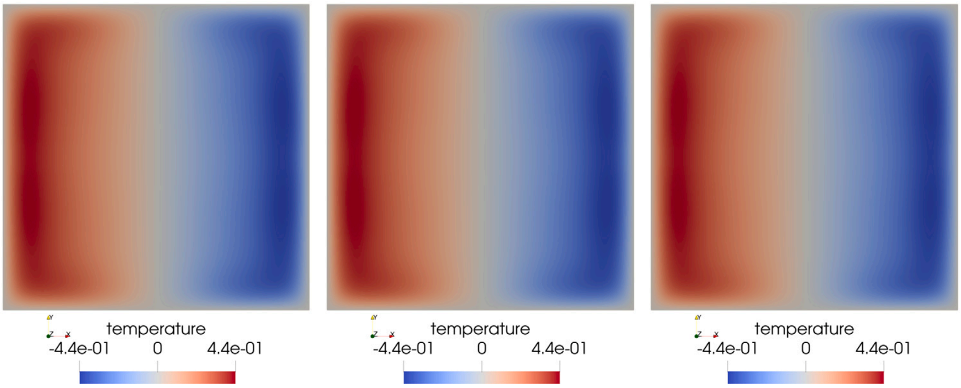

(g) ϑ (monolithic) (h) ϑ (isothermal split) (i) ϑ (adiabatic split)

Fig. 2. Numerical results of the displacement field u_x, u_y, and the relative temperature field ϑ at $t = 100$ when the time increment $\Delta t = 0.5$: (a), (d), (g) are obtained from the monolithic approach that are considered as the reference solutions; (b), (e), (h) are obtained from the staggered approach using the isothermal split; (c), (f), (i) are obtained from the staggered approach using the adiabatic split. When the time step is small, all the numerical techniques produce similar results.

adiabatic split not only maintains the unconditional stability, but also provides numerical results matching the counterparts from the monolithic approach. This unconditional stability is significant when it comes to the modeling of the TBC systems, since it allows the finite element simulation to use large time steps. Moreover, comparing with the monolithic approach, the staggered approach is highly efficient due to the size and the symmetry of the formed linear systems.

4. Thermal barrier coating system

In this section, we use the staggered approach based on the adiabatic split and the monolithic approach respectively to model the transient behavior of a typical thermal barrier coating (TBC) system under an externally imposed thermal gradient. Fig. 8 shows

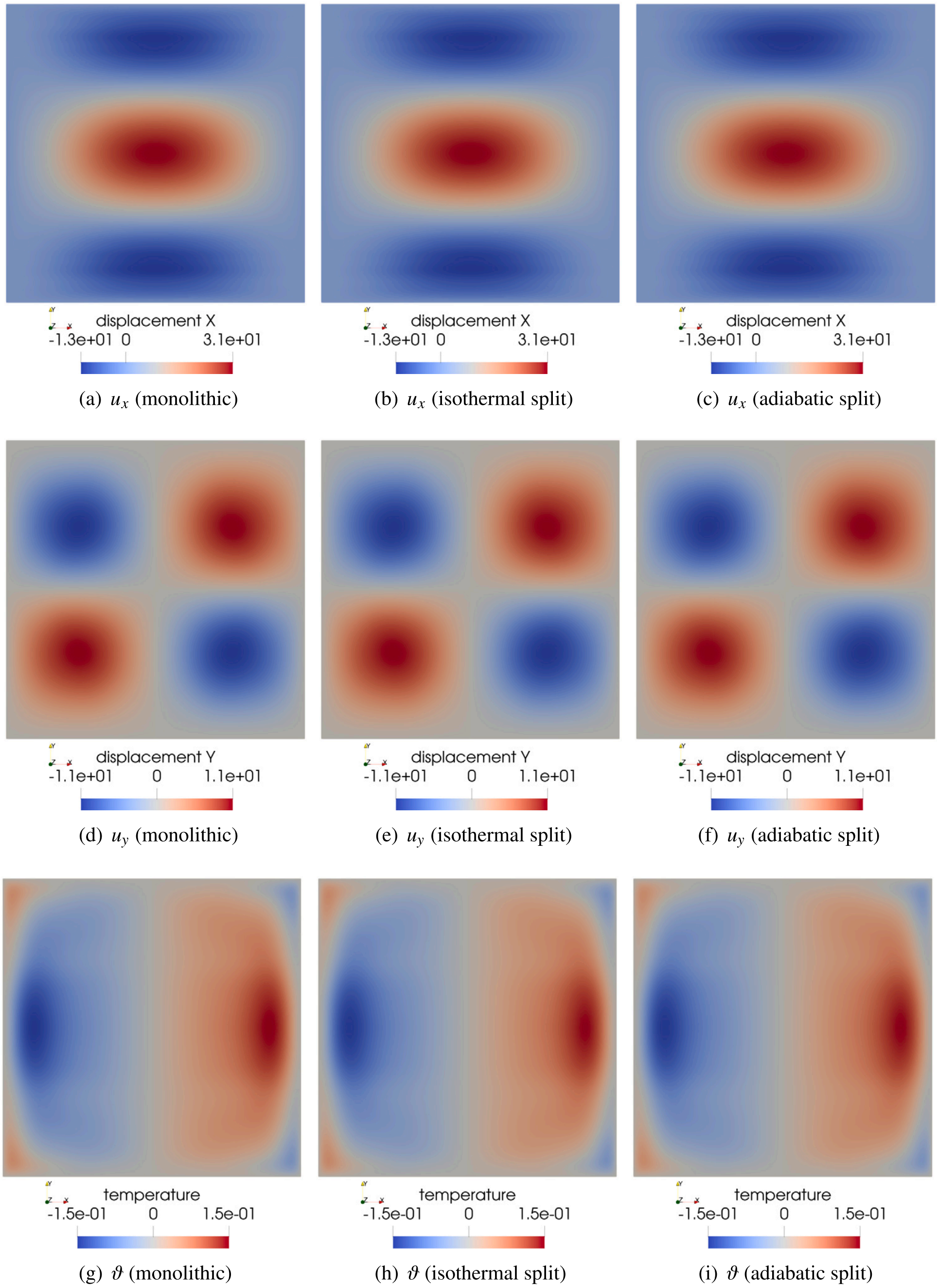

Fig. 3. Numerical results of the displacement field u_x, u_y, and the relative temperature field ϑ at $t = 200$ when the time increment $\Delta t = 0.5$: (a), (d), (g) are obtained from the monolithic approach that are considered as the reference solutions; (b), (e), (h) are obtained from the staggered approach using the isothermal split; (c), (f), (i) are obtained from the staggered approach using the adiabatic split. When the time step is small, all the numerical techniques produce similar results.

the TBC system used in this investigation, which is composed of a top layer with the thickness $H_4 = 100$ μm, a thermally grown oxide (TGO) layer with the thickness $H_3 = 6$ μm, a bond coat layer with the thickness $H_2 = 150$ μm, and a substrate layer with the thickness $H_1 = 1000$ μm. Particularly, the TGO layer is assumed to be sinusoidal with a wavelength $L = 30$ μm and an amplitude $A = 5$ μm. As a result, the TBC system is periodic along the x-direction. In order to effectively resolve the TGO layer that possesses the smallest thickness among all the components without significantly increasing the computational cost, we take advantage of the periodic structure of the TBC system by using a unit wavelength $L = 30$ μm as the computational domain. Meanwhile, the periodic boundary conditions are applied to the left and right edges, as shown in Fig. 8.

In Tables 1 to 4, we report the typical ranges of various material parameters for the four different TBC layers after surveying the literature. The adopted parameter values used in the following numerical simulations are taken from the reported ranges. It is worth

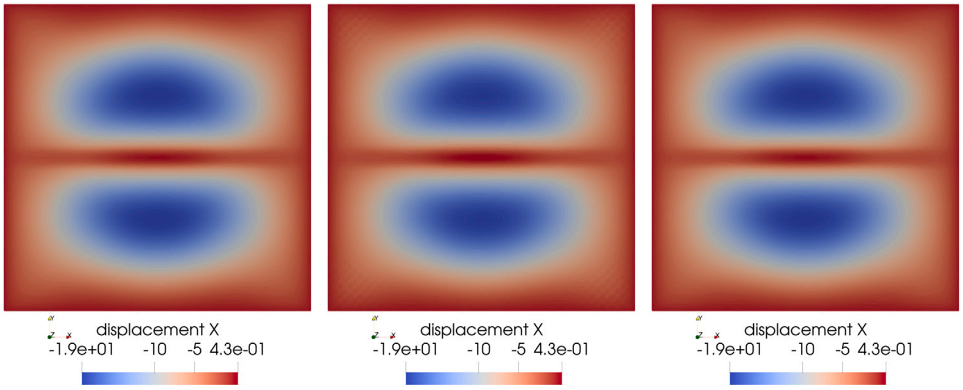

(a) u_x (monolithic) (b) u_x (isothermal split) (c) u_x (adiabatic split)

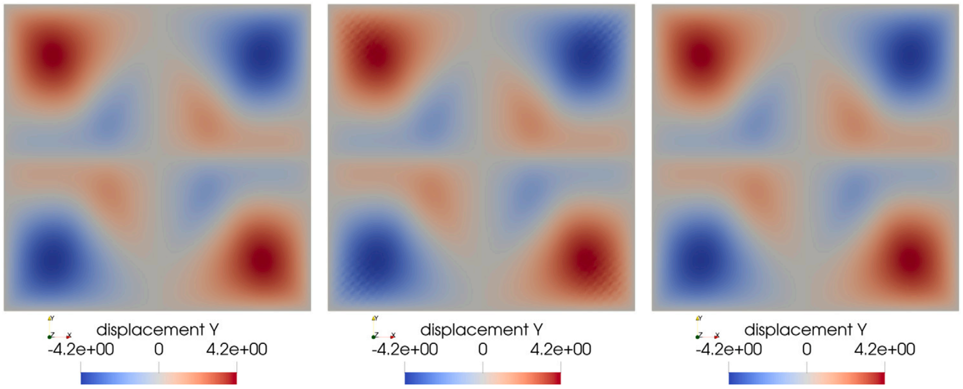

(d) u_y (monolithic) (e) u_y (isothermal split) (f) u_y (adiabatic split)

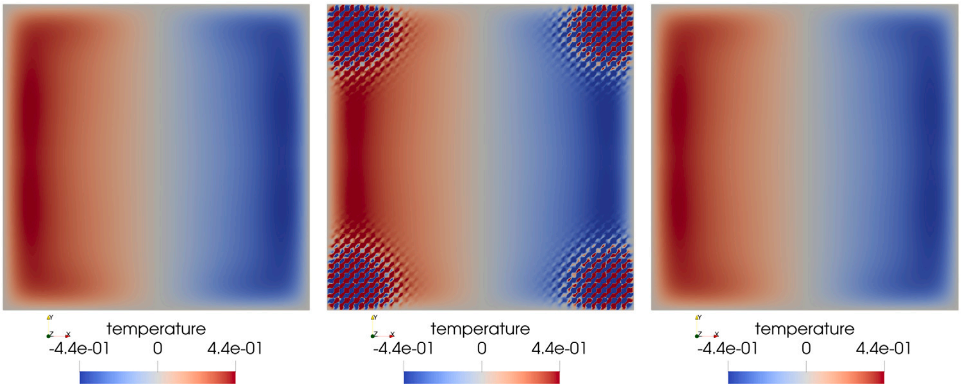

(g) ϑ (monolithic) (h) ϑ (isothermal split) (i) ϑ (adiabatic split)

Fig. 4. Numerical results of the displacement field u_x, u_y, and the relative temperature field ϑ at $t = 100$ when the time increment $\Delta t = 1.0$: (a), (d), (g) are obtained from the monolithic approach that are considered as the reference solutions; (b), (e), (h) are obtained from the staggered approach using the isothermal split; (c), (f), (i) are obtained from the staggered approach using the adiabatic split. When the time step is large, the relative temperature field obtained from the isothermal split becomes unstable. On the other hand, the results based on the adiabatic split are still consistent with the counterparts of the monolithic approach.

emphasizing that many material parameters, such as the Young's modulus, the specific heat capacity, and the thermal conductivity, are temperature-dependent, which means that they have different values depending on the operation temperature. For instance, see the stress analysis in TBC for a rocket engine [33]. For any real-world applications of TBC systems, which typically operate within a large range of temperature (from room temperature to above 1200 °C), it is important to include the temperature-dependency of the material parameters in finite element simulations to obtain realistic numerical results. The current work focuses on demonstrating the unconditional stability and accuracy of the staggered approach, its supremacy regarding the computational efficiency, as well as several finite element simulation techniques such as the adaptive mesh refinement and the periodic boundary conditions in the thermoelastic simulation of TBC system. Therefore, we assume all the material parameters are constant, the specific values of which

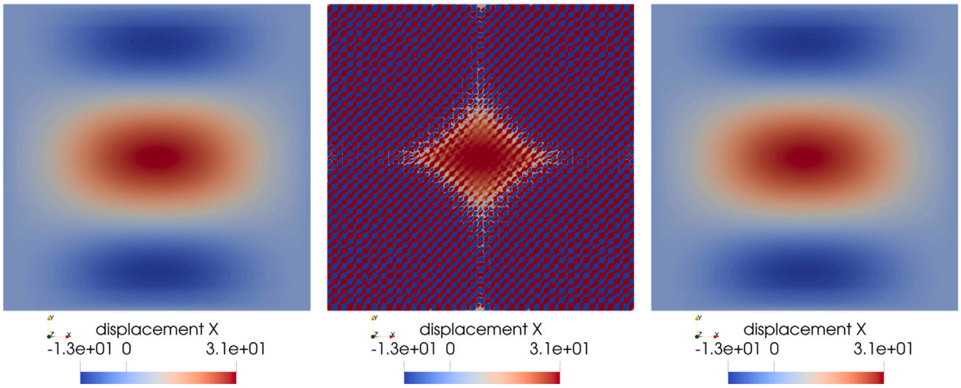

(a) u_x (monolithic) (b) u_x (isothermal split) (c) u_x (adiabatic split)

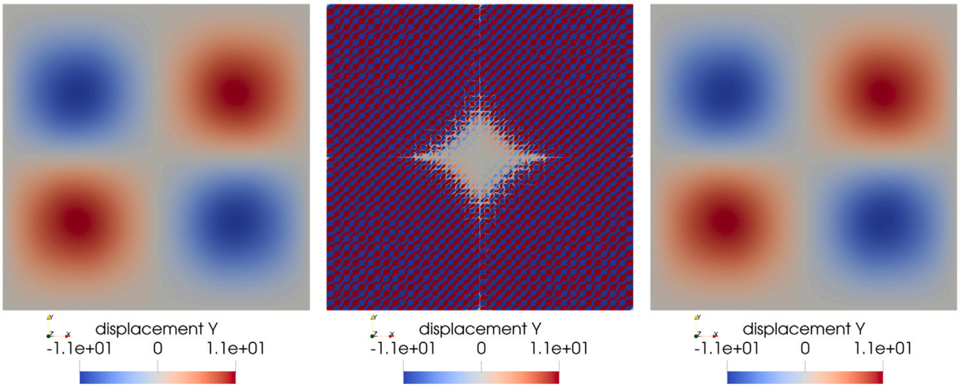

(d) u_y (monolithic) (e) u_y (isothermal split) (f) u_y (adiabatic split)

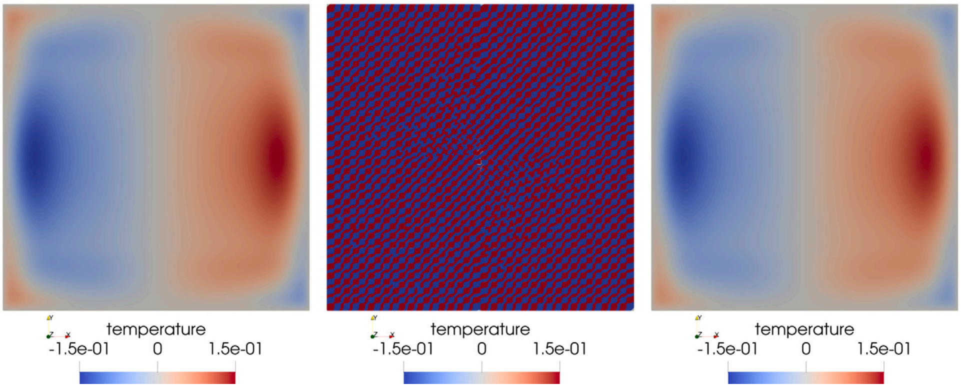

(g) ϑ (monolithic) (h) ϑ (isothermal split) (i) ϑ (adiabatic split)

Fig. 5. Numerical results of the displacement field u_x, u_y, and the relative temperature field ϑ at $t = 200$ when the time increment $\Delta t = 1.0$: (a), (d), (g) are obtained from the monolithic approach that are considered as the reference solutions; (b), (e), (h) are obtained from the staggered approach using the isothermal split; (c), (f), (i) are obtained from the staggered approach using the adiabatic split. When the time step is large, all the results obtained from the isothermal split are unstable. On the other hand, the results based on the adiabatic split are still consistent with the counterparts of the monolithic approach.

are listed in Tables 1 to 4. However, there are no fundamental difficulties to include a series of temperature-dependent material parameters using the technique of parameter interpolations.

The computational cost of a numerical simulation is directly related to the mesh density. Fig. 9(a) shows the initial mesh around the TGO layer at the beginning of the numerical simulation. Due to the mismatch of the thermal expansion coefficients of the top coat, the TGO, and the bond coat layers, a large displacement gradient is expected to develop at the interfaces of these different material layers. Therefore, a more refined mesh around these interfaces are required for more accurate numerical results. In order to increase the accuracy of the numerical simulation without performing global level mesh refinements, the technique of adaptive mesh refinement is adopted. The basic idea of adaptive mesh refinement is to only refine mesh in the regions of interest, in the case of the TBC system,

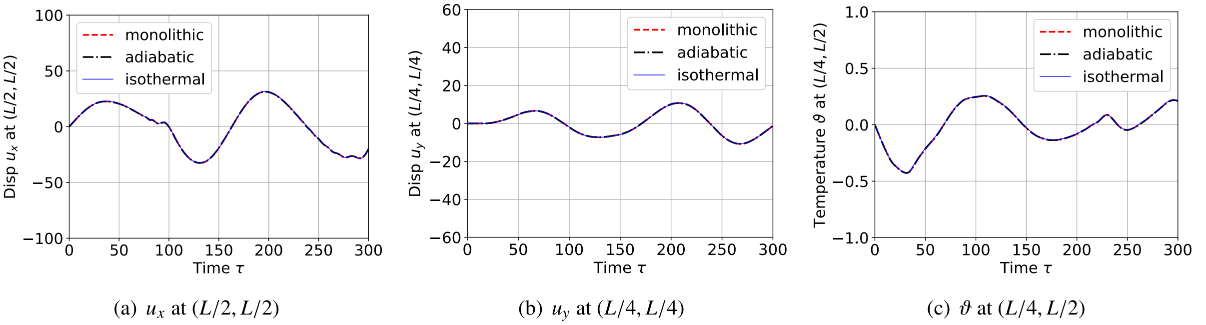

(a) u_x at $(L/2, L/2)$ (b) u_y at $(L/4, L/4)$ (c) ϑ at $(L/4, L/2)$

Fig. 6. The time history of (a) u_x at $(L/2, L/2)$, (b) u_y at $(L/4, L/4)$, and (c) ϑ at $(L/4, L/2)$ when the time step size is $\Delta t = 0.5$. All the numerical results obtained from the monolithic approach and the two staggered approaches using the isothermal split and the adiabatic split are similar.

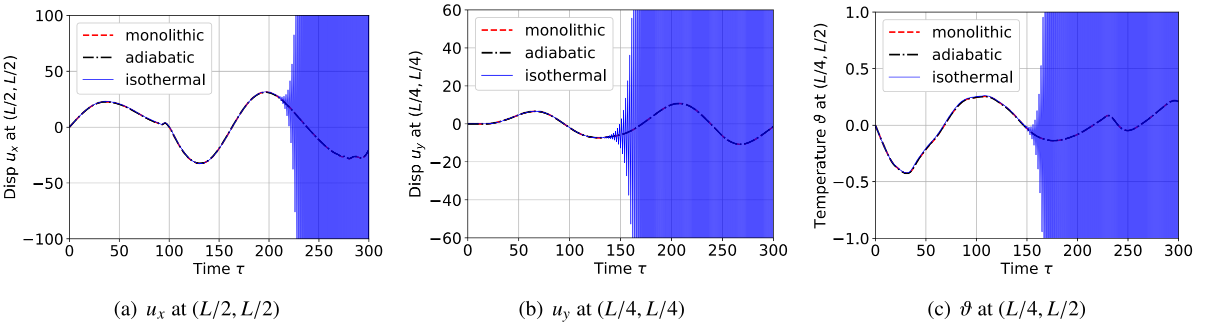

(a) u_x at $(L/2, L/2)$ (b) u_y at $(L/4, L/4)$ (c) ϑ at $(L/4, L/2)$

Fig. 7. The time history of (a) u_x at $(L/2, L/2)$, (b) u_y at $(L/4, L/4)$, and (c) ϑ at $(L/4, L/2)$ when the time step size is $\Delta t = 1.0$. The numerical results obtained from the adiabatic split still match the counterparts obtained from the monolithic approach. However, the numerical results obtained from the isothermal split become unstable.

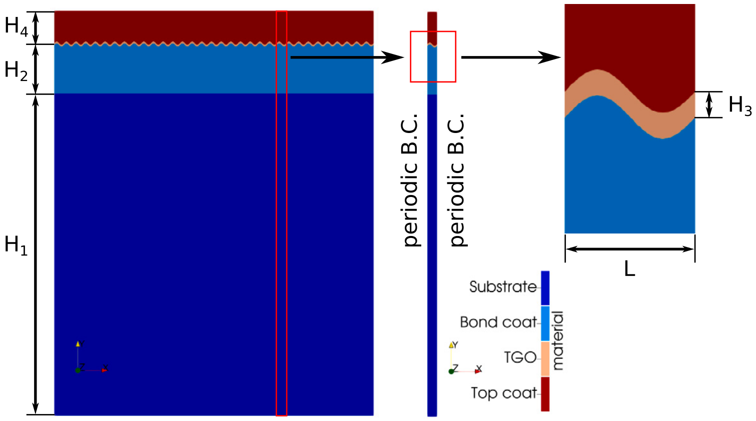

Fig. 8. A typical TBC system has four layers with different thicknesses, including a top coat layer ($H_4 = 100$ μm), a thermally grown oxide (TGO) layer ($H_3 = 6$ μm), a bond coat layer ($H_2 = 150$ μm), and a substrate layer ($H_1 = 1000$ μm). The TGO layer is assumed to have a sinusoidal shape with a wavelength $L = 30$ μm and an amplitude $A = 5$ μm. Due to the periodic structure, the computational domain only contains one sinusoidal period with the periodic boundary conditions applied on the left and right edges.

the regions exhibiting large levels of stress concentration. In this work, we adopt the paradigm of “solve-estimate-mark-refine” as the adaptive mesh refinement strategy. In this paradigm, the “solve” stage means to solve the thermomechanically coupled finite element problem using either the monolithic approach or the staggered approach. Once the finite element solution is obtained from the “solve” stage, the following “estimate” stage is to estimate the error associated with each element based on a prescribed criterion. Then, the “mark” stage is to mark the elements with large error indicators for refinement. Lastly, the “refine” stage is to execute the mesh refinement based on the element labels (“refine” or “unchanged”) provided during the “mark” stage. According to the paradigm of “solve-estimate-mark-refine”, a reliable error estimator is crucial to a successful adaptive mesh refinement technique. In this work, an error estimator based on the so-called Kelly error estimator [47] is adopted. This error estimator attempts to approximate the error per element by integrating the jump of the solution gradient along the faces of each element [32]. Since we are interested in

Table 1
Dimension and material parameters of the top coat layer (7YSZ or YSZ, partially yttria-stabilized zirconia), data sources: [34–37,1,38].

	Reported range	Adopted value
Thickness (μm)	$100 \sim 250$	100
Young's modulus (GPa)	$0.72 \sim 2.3$	2.3
Poisson ratio	0.23	0.23
Density ($\mathrm{g \cdot cm^{-3}}$)	$3.38 \sim 4.50$	3.38
Thermal expansion coeff. ($\mathrm{K^{-1}}$)	$10.0 \sim 12.0 \times 10^{-6}$	11.0×10^{-6}
Thermal conductivity ($\mathrm{W \cdot m^{-1} \cdot K^{-1}}$)	$1.5 \sim 1.9$	1.5
Specific heat capacity ($\mathrm{J \cdot g^{-1} \cdot K^{-1}}$)	$0.44 \sim 0.65$	0.5

Table 2
Dimension and material parameters of the thermally grown oxide (TGO) layer (predominantly α-$\mathrm{Al_2O_3}$), data sources: [39]; MatWeb[1].

	Reported range	Adopted value
Thickness (μm)	$1 \sim 10$	6
Young's modulus (GPa)	$260 \sim 340$	300
Poisson ratio	0.22	0.22
Density ($\mathrm{g \cdot cm^{-3}}$)	3.95	3.95
Thermal expansion coeff. ($\mathrm{K^{-1}}$)	$7.6 \sim 8.2 \times 10^{-6}$	8.0×10^{-6}
Thermal conductivity ($\mathrm{W \cdot m^{-1} \cdot K^{-1}}$)	$12.0 \sim 30.0$	25.0
Specific heat capacity ($\mathrm{J \cdot g^{-1} \cdot K^{-1}}$)	0.88	0.88

[1] https://www.matweb.com/search/DataSheet.aspx?MatGUID=0654701067d147e88e8a38c646dda195.

Table 3
Dimension and material parameters of the bond coat layer (primarily NiCoCrAlY), data sources: [40–42,1,43].

	Reported range	Adopted value
Thickness (μm)	$100 \sim 200$	150
Young's modulus (GPa)	$130 \sim 220$	220
Poisson ratio	0.3	0.3
Density ($\mathrm{g \cdot cm^{-3}}$)	7.32	7.32
Thermal expansion coeff. ($\mathrm{K^{-1}}$)	$14.0 \sim 17.5 \times 10^{-6}$	14.0×10^{-6}
Thermal conductivity ($\mathrm{W \cdot m^{-1} \cdot K^{-1}}$)	4.3	4.3
Specific heat capacity ($\mathrm{J \cdot g^{-1} \cdot K^{-1}}$)	0.501	0.501

Table 4
Dimension and material parameters of the substrate layer (Ni-based superalloy), data sources: [44–46].

	Reported range	Adopted value
Thickness (μm)	≥ 1000	1000
Young's modulus (GPa)	$106 \sim 225$	200
Poisson ratio	0.3	0.3
Density ($\mathrm{g \cdot cm^{-3}}$)	8.9	8.9
Thermal expansion coeff. ($\mathrm{K^{-1}}$)	$17.0 \sim 18.0 \times 10^{-6}$	18.0×10^{-6}
Thermal conductivity ($\mathrm{W \cdot m^{-1} \cdot K^{-1}}$)	$9.8 \sim 29.5$	29.5
Specific heat capacity ($\mathrm{J \cdot g^{-1} \cdot K^{-1}}$)	$0.44 \sim 0.67$	0.6

refining regions with large stress concentration, we can define the Kelly error estimator based on the gradient of the displacement field solved from the finite element procedure. Inside the Kth element (assume the element is 2D), the error estimator η_K, which is a scalar, is defined as

$$\eta_K = \sqrt{\sum_{F \in \partial\Omega^{(K)}} c_F \int_{\partial\Omega^{(K)}} \left(\left[\left[\boldsymbol{\nabla} u_x \cdot \boldsymbol{n} \right]\right]^2 + \left[\left[\boldsymbol{\nabla} u_y \cdot \boldsymbol{n} \right]\right]^2 \right) \mathrm{d}A}, \tag{29}$$

where $\partial\Omega^{(K)}$ represents the element boundary, $\boldsymbol{n}$ represents the normal direction of the element boundary, the coefficient c_F is chosen as $h_K/24$ [32,47], and h_K is the element largest diagonal length. Since stress is proportional to strain or displacement gradient, the above error estimator is capable of properly reflecting the level of stress concentration. A large error estimator η_K indicates that there is a large change of stresses across element boundaries, and therefore, such an element should be refined to provide a better

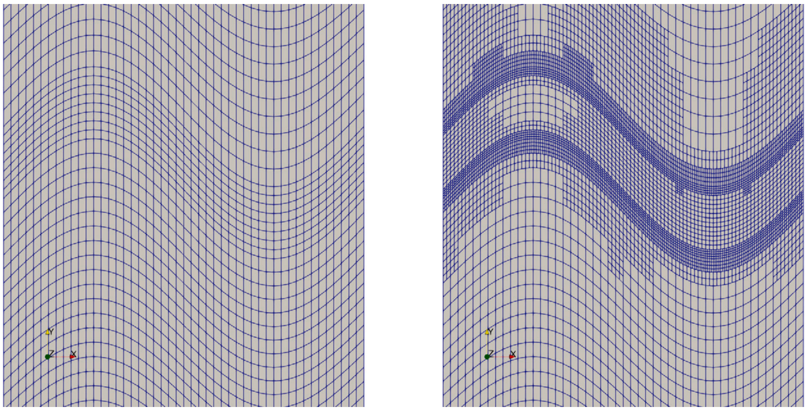

(a) Initial mesh (b) Adaptively refined mesh

Fig. 9. Adaptive mesh refinement based on the Kelly refinement indicator is applied in the numerical simulation. (a) The initial coarse mesh is adopted at the beginning of the simulation. (b) Due to the mismatch of the thermal expansion coefficients β at the interface between the top coat layer and the TGO layer, as well as the interface between the TGO layer and the bond coat layer, large displacement gradients are generated in these areas and cause local adaptive mesh refinement.

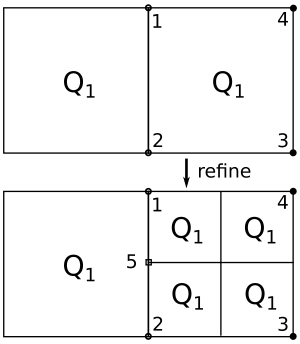

Fig. 10. Degrees of freedom (DoF) associated with a hanging node during the adaptive mesh refinement is treated as a constraint in the assembled linear system.

spatial resolution. For more information about the error estimator, interested readers are referred to the survey by Ainsworth and Oden [48] for a complete discussion. By using the above error estimator, the error η_K can be calculated for each element during the "estimate" stage. During the "mark" stage, all the elements can be ranked according to their error estimator η_K from high to low. The top 10% elements, for example, are labeled for refinement. Then, in the "refine" stage, the refinement is executed according to the above element labels.

Fig. 9(b) shows an adaptively refined mesh based on the paradigm of the "solve-estimate-mark-refine" approach. Obviously, there exist neighboring elements that are at different refinement levels. For example, an element is one-level more refined than its neighbor. As a result, there are so-called "hanging nodes" generated at the element interfaces during the mesh refinement process. For instance, in Fig. 10, the right element is refined one more level than the left element during the adaptive mesh refinement process, resulting in a hanging node at the interface. The degree of freedom associated with this hanging node generated during the adaptive mesh refinement is treated as an algebraic constraint in the assembled linear system. Assume that both elements use the bilinear (Q1) interpolation functions. Then, the unknown u_5 associated with the hanging node (node 5) can be expressed by the unknowns u_1 and u_2 associated with the neighboring nodes (nodes 1 and 2) in the following linear relationship,

$$u_5 = \frac{1}{2}u_1 + \frac{1}{2}u_2. \tag{30}$$

On the other hand, if node 4 is prescribed with an essential (Dirichlet) boundary condition, then the DoF of u_4 associated with this node can be written as

$$u_4 = g_4, \tag{31}$$

where g_4 represents the prescribed boundary value.

As discussed previously, the computational domain is part of the TBC system containing one sinusoidal wavelength, as shown in Fig. 8. The left and right edges are applied with the periodic boundary conditions on the velocity, the displacement, and the temperature fields. Let $\boldsymbol{u}_{\text{left}}$ represent the finite element nodal solutions at the left edge of the computational domain and $\boldsymbol{u}_{\text{right}}$

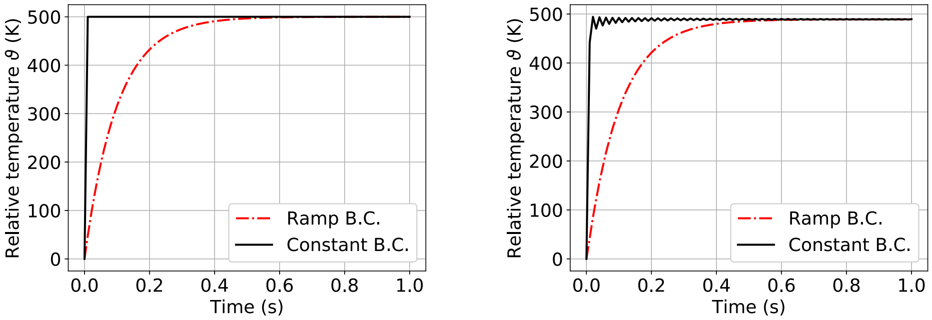

(a) Applied B.C. at the top surface (b) Temperature near the top surface

Fig. 11. Influence of (a) the applied relative temperature boundary conditions at the top surface of TBC (constant temperature vs. ramp temperature) on (b) the evolution of the temperature near the top surface. Notice that the room temperature 300 K is set as the reference temperature $\Theta_{\text{ref}} = 300$ K. Therefore, the applied absolute temperature boundary condition at the top surface is 800 K.

represent the counterparts at the right edge of the computational domain. Due to the imposed periodic boundary conditions on both edges, we have the following relationship

$$\boldsymbol{u}_{\text{left}} = \boldsymbol{u}_{\text{right}}. \tag{32}$$

The linear relationships due to the hanging-node constraints as shown in Eq. (30), the ones due to the prescribed essential (Dirichlet) boundary conditions as shown in Eq. (31), and the ones due to the imposed periodic boundary conditions as shown in Eq. (32) can be expressed in the following general linear form:

$$u_i = c_{ij} u_j + g_i,$$

where c_{ij} represents the coefficients due to the hanging-node constraints as well as the periodic boundary conditions, and g_i represents the inhomogeneous constraints such as the essential boundary conditions. We can write the entire constraints in a linear system as below:

$$\boldsymbol{u} = \mathbf{C}\boldsymbol{u} + \boldsymbol{g}.$$

Particularly, the coefficient matrix $\mathbf{C}$ is idempotent, meaning that $\mathbf{C}^2 = \mathbf{C}$, and the proof of which can be found in [49]. After the linear system $\mathbf{K}\boldsymbol{u} = \boldsymbol{F}$ is assembled according to either the monolithic approach or the staggered approach, in order to consider the above set of constraints, we can instead solve the following modified linear system [50]

$$\left(\mathbf{C}^{\mathrm{T}}\mathbf{K}\mathbf{C} + \mathbf{I}_{d_c}\right)\hat{\boldsymbol{u}} = \mathbf{C}^{\mathrm{T}}\left(\boldsymbol{F} - \mathbf{K}\boldsymbol{g}\right) \tag{33}$$

and then recover the true solution $\boldsymbol{u}$ as

$$\boldsymbol{u} = \mathbf{C}\hat{\boldsymbol{u}} + \boldsymbol{g}. \tag{34}$$

In the modified linear system, the matrix $\mathbf{I}_{d_c}$ is defined as

$$(\mathbf{I}_{d_c})_{ij} = \begin{cases} 0 & \text{if} \quad i \neq j, \\ 1 & \text{if} \quad i = j \in \mathcal{T}, \\ 0 & \text{if} \quad i = j \notin \mathcal{T}, \end{cases} \tag{35}$$

where $\mathcal{T}$ represents the set of DoFs of the constrained nodes, including the hanging nodes and the nodes prescribed with the periodic boundary conditions as well as the essential (Dirichlet) boundary conditions. Obviously, for a linear system without any nodal constraints, we have $\mathbf{C} = \mathbf{I}$, $\mathbf{I}_{d_c} = \mathbf{0}$, and $\boldsymbol{g} = \mathbf{0}$.

We assume the room temperature 300 K as the reference temperature Θ_{ref}. At the bottom edge of the computational domain, the velocity field $\boldsymbol{v}$ and the displacement field $\boldsymbol{u}$ are fixed, and the relative temperature ϑ is assumed to be zero (absolute temperature 300 K) as the temperature boundary condition. At the top surface, the relative temperature $\vartheta = 500$ K (absolute temperature 800 K) is applied as the boundary condition. The initial values of all the unknown fields are zero.

When the relative temperature boundary condition $\vartheta = 500$ K (the absolute temperature $\vartheta + \Theta_{\text{ref}} = 800$ K) is instantly applied as a constant to the top surface of the TBC system, as shown in Fig. 11(a), the temperature field near the top surface solved by the Crank-Nicolson method exhibits a noticeable oscillatory behavior due to the sharp initial transient response, as shown in Fig. 11(b). This oscillatory behavior is well documented in the literature, see [51,52]. In this example, we adopt a simple approach proposed by Wood [51] to alleviate this oscillatory behavior by applying the temperature boundary condition in a ramp manner,

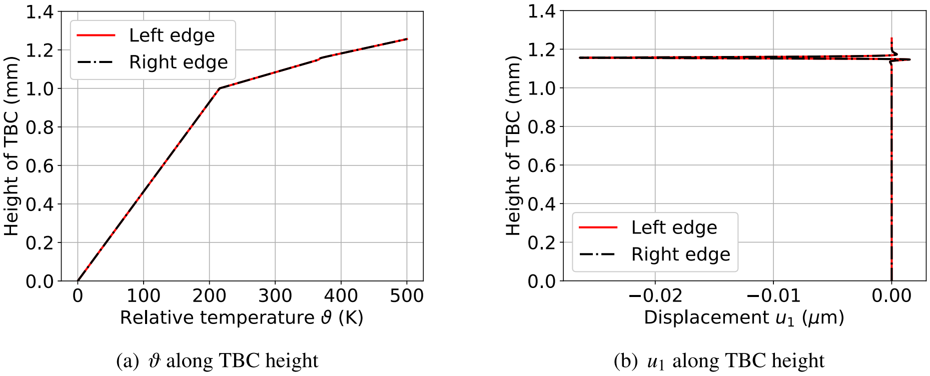

(a) ϑ along TBC height (b) u_1 along TBC height

Fig. 12. Distributions of (a) the relative temperature ϑ and (b) the displacement u_1 along the height of the TBC system. Due to the applied periodic boundary conditions, the results obtained from the left edge and the right edge overlap.

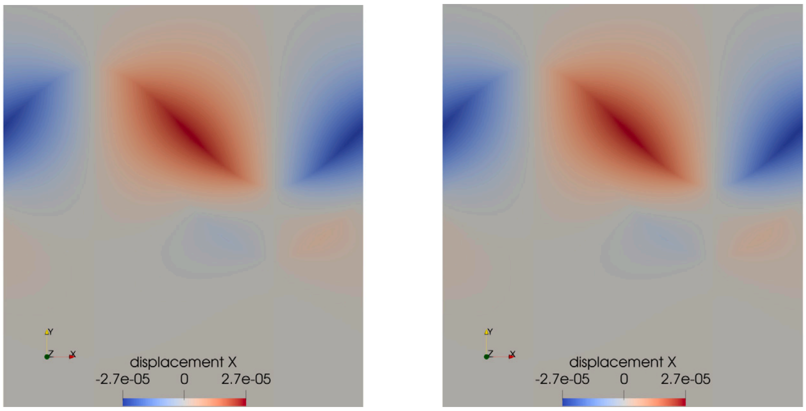

(a) Disp. u_1 (adiabatic solve) (b) Disp. u_1 (monolithic solve)

Fig. 13. Displacement u_1 (unit: mm) at the interface between the top coat and the TGO, and at the interface between the bond coat and the TGO obtained from (a) the adiabatic split solve and (b) the monolithic solve.

$$\vartheta(t) = \vartheta_0(1 - e^{-\beta t}),$$

where ϑ_0 is the initial temperature and β is a parameter controlling how fast the temperature at the boundary reaches to the targeted value. We set the parameter β as 10. Then, the temperature at the top surface is smoothly increased to the targeted value as the boundary condition, as shown in Fig. 11(a). Correspondingly, the oscillatory response near the boundary disappears, as shown in Fig. 11(b).

Under the aforementioned boundary conditions, Fig. 12 shows the solutions along the height of the TBC system after the transient problem reaches to the steady-state. Due to the prescribed periodic boundary conditions, the solutions along the left edge and the right edge of the computational domain overlap. From Fig. 12(a), we can see that a larger temperature gradient exists between the top coat layer and the bond coat layer, effectively reducing the temperature inside the substrate layer. Also, because of the mismatch of the thermal expansion coefficients of the top coat, the TGO, and the bond coat layers, a large localized displacement field is generated inside the TGO layer, as shown in Fig. 12(b) and Fig. 13. The localized displacement field further results in large stress concentrations along the interface between the top coat layer and the TGO layer, as well as the interface between the TGO layer and the bond coat layer, as shown in Fig. 14. Even though the specific values of the stress distribution are slightly different from various work in the literature, for instance, see [8,53,54], however, this is not surprising since the finite element results depend on the specific setup of the finite element model, including the adopted material parameters, the sample geometry, and the applied boundary conditions. In fact, the pattern of the obtained stress concentration is consistent with the results reported in the aforementioned work [8,53,54].

Fig. 15 demonstrates the distributions of the stress component σ_{22} at the interface between the top coat and the TGO as well as at the interface between the bond coat and the TGO obtained using different adaptively refined meshes. Even though mesh size has an impact on the magnitudes of the tensile and compressive stresses at these interfaces, the stress distribution around the TGO region follows the same pattern regardless of the underlying mesh. Fig. 16 illustrates the impact of the applied relative temperature boundary condition at the top surface of the TBC system on the stress concentration around the TGO layer. Recall that the room temperature is set as the reference temperature ($\Theta_{\text{ref}} = 300$ K). When the applied relative temperature ϑ is increased from 500 K to 900 K (the absolute temperature is increased from 800 K to 1200 K), the level of stress concentration becomes even more prominent

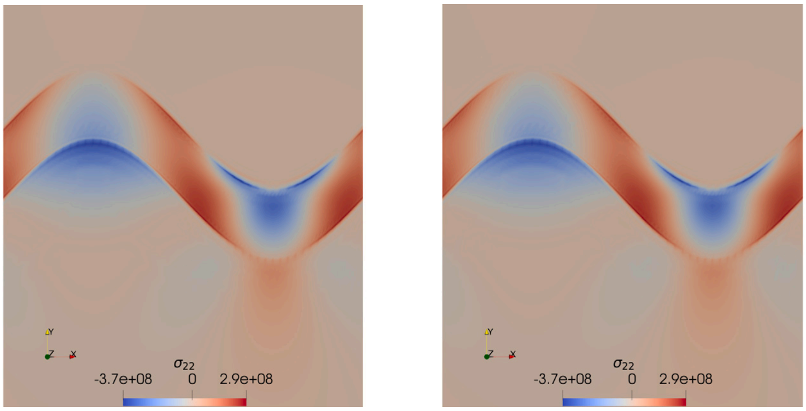

(a) Stress σ_{22} (adiabatic solve) (b) Stress σ_{22} (monolithic solve)

Fig. 14. Distributions of the stress component σ_{22} (unit: Pa) at the interface between the top coat and the TGO, and at the interface between the bond coat and the TGO obtained from (a) the adiabatic split solve and (b) the monolithic solve.

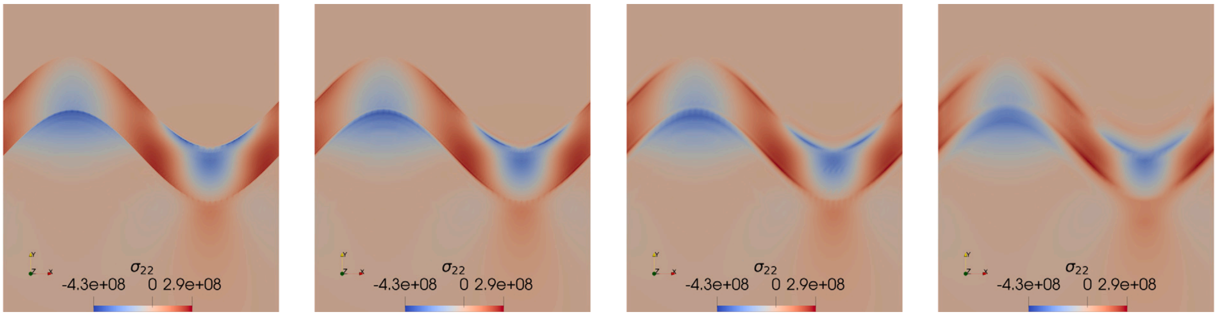

(a) σ_{22} (23328 elmts) (b) σ_{22} (18108 elmts) (c) σ_{22} (14604 elmts) (d) σ_{22} (12396 elmts)

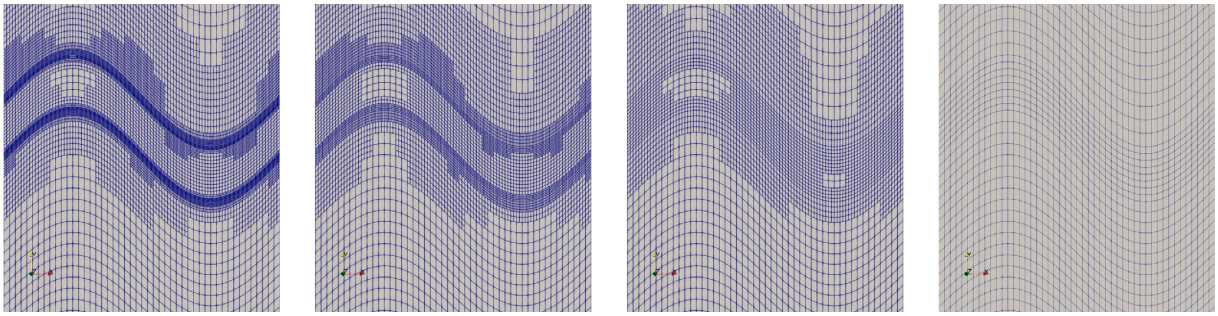

(e) Mesh (23328 elmts) (f) Mesh (18108 elmts) (g) Mesh (14604 elmts) (h) Mesh (12396 elmts)

Fig. 15. Distributions of the stress component σ_{22} (unit: Pa) (a, b, c, d) at the interface between the top coat and the TGO as well as at the interface between the bond coat and the TGO obtained using different adaptively refined meshes (e, f, g, h). Even though mesh size has an impact on the magnitudes of the tensile and compressive stresses, the stress distribution around the TGO region follows the same pattern regardless of the underlying mesh.

around the TGO layer. This is expected since a higher temperature field means that a larger strain field is generated at the interfaces between the TGO and neighboring layers due to the mismatch of their thermal expansion coefficients.

The thermomechanically coupled behaviors of the TBC system are simulated using the monolithic approach and the staggered approach based on the adiabatic split, respectively. The steady-state solutions of the displacement field and the stress field around the TGO layer obtained from these two approaches are compared in Figs. 13 and 14. We can see that the two approaches obtain matching results. However, the staggered approach based on the adiabatic split not only preserves the unconditional stability from individual time integration techniques (the Crank-Nicolson method and the backward Euler method) for the mechanical phase and the thermal phase, but also provides appealing computational efficiency compared with the monolithic approach. Table 5 reports the number of degrees of freedom and the computational cost related with the linear solve of the assembled global system from the monolithic approach and the staggered approach based on the adiabatic split. The linear solver is a sparse direct solver UMFPACK, which is part of the SuiteSparse library. The simulations are run in the same workstation with 11th Gen Intel(R) Core$^{\mathrm{TM}}$ i7-11800H

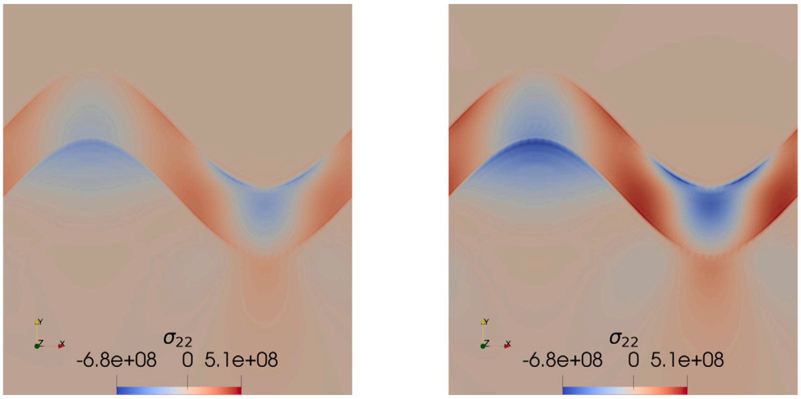

(a) Stress σ_{22} (ϑ = 500 K) (b) Stress σ_{22} (ϑ = 900 K)

Fig. 16. Impact of the applied relative temperature boundary condition (the reference temperature is $\Theta_{\text{ref}} = 300$ K) at the top surface on the distributions of the stress component σ_{22} (unit: Pa) around the TGO layer: (a) when $\vartheta = 500$ K (the absolute temperature is 800 K) and (b) when $\vartheta = 900$ K (the absolute temperature is 1200 K). The level of stress concentration around the TGO layer is even more prominent when a larger relative temperature ($\vartheta = 900$ K) is applied at the top surface of the TBC system.

Table 5
Computational cost related with the sparse direct solver UMFPACK[1] for the monolithic approach and the staggered approach used for the finite element simulation of the TBC system.

	No. DoFs	Time per solve (s)
Monolithic	83500	264.0
Adiabatic split	75548 (mechanical phase)	0.853
	18887 (thermal phase)	0.047

[1] https://people.engr.tamu.edu/davis/suitesparse.html.

@ 2.30 GHz × 16. From Table 5, we can see that even the linear system assembled from the monolithic approach is only slightly larger than the counterpart of the mechanical phase in the staggered approach, it takes significantly more time per linear solve. This is partly because the linear system of the monolithic approach is unsymmetric, as shown in the block matrices of Eq. (15). Moreover, part of the diagonal block matrices $\mathbf{K}_{vv}$ and $\mathbf{K}_{uu}$ are derived from one type of physics, in this case, the mechanics, while the other part of the diagonal block matrix $\mathbf{K}_{\vartheta\vartheta}$ is derived from a different type of physics, in this case, the heat conduction. These diagonal block matrices have drastically different magnitudes. Therefore, an effective preconditioner would be required to lower the condition number of the monolithic system in order to reduce the computational cost, provided an iterative linear solver is adopted. On the other hand, the assembled linear systems of the two sub-problems from the staggered approach are both symmetric and have smaller sizes. Also, each linear system is derived from one type of physics, namely, the mechanics and the heat conduction, respectively. As a result, the computational cost associated with the linear solving stage in the staggered approach is significantly lower. When the three-dimensional finite element simulation of the TBC system containing a large number of DoFs (above 10^6) under long-term cyclic thermal loading conditions is required to investigate its transient thermomechanical behavior in real-world applications, the preserved unconditional stability from individual time integration techniques and the computational efficiency of the staggered approach based on the adiabatic split provide significant advantages.

5. Conclusions and future work

In this paper, we present in detail several numerical approaches to simulate the transient behavior of thermomechanically coupled systems, including a monolithic approach and two staggered approaches based on the isothermal split and the adiabatic split, respectively. The provided block matrices in each assembled linear system facilitate the finite element implementation in both open-source and commercial finite element packages. More importantly, we apply the above numerical approaches to investigate the thermomechanical behavior of a thermal barrier coating (TBC) system containing a multi-layer structure. Particularly, we demonstrate several finite element simulation techniques, such as the periodic boundary conditions and the adaptive mesh refinement, which are crucial to obtain accurate simulation results with a reasonable computational cost. In addition, we demonstrate the impact of stiff boundary conditions on the numerical results when the Crank-Nicolson method is applied, and subsequently how to mitigate the oscillatory responses via a simple technique. By comparing the numerical results obtained from the staggered approach based on the adiabatic split and the monolithic approach, as well as their computational costs, we show that the adiabatic split not only preserves the unconditional stability of individual time integration techniques for the mechanical and thermal sub-problems, but also provide the significant computation efficiency. These advantages are especially appealing in the three-dimensional finite element simulation of

TBC systems under long-term cyclic thermal loading conditions, which not only contains a large number of degrees of freedom but also requires large time steps.

In the provided numerical examples, we only focus on the thermoelastic behavior of the TBC systems. However, we recognize that these systems are highly complex and experience continuously changing composition, crystalline phases, and microstructures in real-world service conditions. For example, the TGO layer growth over time is one of the leading factors resulting in failure and limiting the lifespan of the TBC system. Typically, the increasing thickness of the TGO layer due to the gradual oxidization happens over long term. In order to reliably simulate the growth of the TGO layer, we believe that there are at least two modeling challenges. First, we need a proper multiphysics model to describe the governing law of the TGO layer growth. Such a model could be highly complex due to its multiphysics nature. Second, we need a proper numerical scheme that is unconditionally stable, so that we can take large time steps during the numerical simulation of the TGO growth that is generally a long-term phenomenon. The current paper focuses on tackling the second challenge. We demonstrate that the staggered approach based on the adiabatic split can preserve the unconditional stability offered by various time integration techniques such as the backward Euler method and the Crank-Nicolson method. This feature would allow us to take large time steps during the investigation of the long-term behavior of the TBC system. Also, comparing with the monolithic approach, the staggered approach can significantly reduce the computational cost. Both advantages are crucial for the numerical investigation of the TGO growth.

In our ongoing research, we are actively exploring various options to incorporate the TGO growth model into our current computational framework. Some examples of the TGO growth model include the work done by Zhou et al. [27], Min et al. [28], Xiao et al. [29]. Since the mechanism of the TGO growth is highly complex, our goal is to achieve a balance between the model simplicity and accuracy. Once a proper governing law of the TGO growth is formulated, we believe our current staggered approach can be extended to investigate the TGO growth in a fully coupled chemo-thermo-mechanical framework. Besides the growth of the TGO layer, the bond coat experiences phase transformations due to Al depletion and inter-diffusion between the bond coat and the substrate. There are various damage mechanisms causing TBC to degrade and fail, which are among the most concerned topics in the field of TBC research. For instance, the stress concentration at the interface between the TGO and neighboring layers usually leads to the delamination and spallation failure of TBC systems. Even though the numerical simulations in the current work are only thermoelastic, the obtained locations of the stress concentration are still crucial for our future investigation about the TBC failure modeling, since these locations typically indicate the locations of crack initiation. One of our ongoing research efforts is to combine the unconditionally stable staggered approach with some crack propagation modeling techniques, such as the stress-based cohesive zone model and the energy-based phase-field model. These topics will be further pursued in our future research with the help of the unconditionally stable staggered time integration approach presented in this work.

CRediT authorship contribution statement

Zhao Li: Writing – review & editing, Writing – original draft, Visualization, Software, Methodology, Formal analysis. **Kuiying Chen:** Writing – review & editing, Validation, Resources, Investigation, Funding acquisition, Conceptualization. **Tao Jin:** Writing – review & editing, Writing – original draft, Supervision, Methodology, Investigation, Funding acquisition, Formal analysis.

Declaration of competing interest

The authors declare that they have no known competing financial interests or personal relationships that could have appeared to influence the work reported in this paper.

Acknowledgements

Tao Jin is supported by the Natural Sciences and Engineering Research Council of Canada (NSERC) under the Discovery Grants Program (funding reference number: RGPIN-2021-02561). Kuiying Chen is supported by the National Research Council Canada DTS-SCS program A1-018177 project. Their supports are greatly appreciated.

Data availability

Source code of the developed numerical method is hosted on GitHub: https://github.com/taojinllnl/SmallDeformationThermoMechanicalCoupling.

References

[1] R. Darolia, Thermal barrier coatings technology: critical review, progress update, remaining challenges and prospects, Int. Mater. Rev. 58 (2013) 315–348, https://doi.org/10.1179/1743280413Y.0000000019.

[2] A. Pakseresht, M. Saremi, H. Omidvar, M. Alizadeh, Micro-structural study and wear resistance of thermal barrier coating reinforced by alumina whisker, Surf. Coat. Technol. 366 (2019) 338–348, https://doi.org/10.1016/j.surfcoat.2019.03.059.

[3] F. Sun, X. Fan, T. Zhang, P. Jiang, J. Yang, Numerical analysis of the influence of pore microstructure on thermal conductivity and Young's modulus of thermal barrier coating, Ceram. Int. 46 (2020) 24326–24332, https://doi.org/10.1016/j.ceramint.2020.06.214.

[4] Q.-L. Xu, K.-C. Liu, K.-Y. Wang, L.-Y. Lou, Y. Zhang, C.-J. Li, C.-X. Li, TGO and Al diffusion behavior of CuAlxNiCrFe high-entropy alloys fabricated by high-speed laser cladding for TBC bond coats, Corros. Sci. 192 (2021) 109781, https://doi.org/10.1016/j.corsci.2021.109781.

[5] P. Seiler, M. Bäker, J. Rösler, Influence of creep and cyclic oxidation in thermal barrier coatings, Int. J. Mater. Res. 103 (2012) 50–56, https://doi.org/10.3139/146.110629.

[6] R.J. Takahashi, J.M.K. Assis, F.P. Neto, D.A.P. Reis, Heat treatment for TGO growth on NiCrAlY for TBC application, Mater. Res. Express 6 (2020) 126442, https://doi.org/10.1088/2053-1591/ab6778.

[7] M. Ramesh, K. Marimuthu, P. Karuppuswamy, L. Rajeshkumar, Microstructure and properties of YSZ-Al2O3 functional ceramic thermal barrier coatings for military applications, Bol. Soc. Esp. Cerám. Vidr. 61 (2022) 641–652, https://doi.org/10.1016/j.bsecv.2021.06.004.

[8] B. Li, X. Fan, K. Zhou, T. Wang, Effect of oxide growth on the stress development in double-ceramic-layer thermal barrier coatings, Ceram. Int. 43 (2017) 14763–14774, https://doi.org/10.1016/j.ceramint.2017.07.218.

[9] B. Zhang, K. Chen, N. Baddour, P.C. Patnaik, Life prediction of atmospheric plasma-sprayed thermal barrier coatings using temperature-dependent model parameters, J. Therm. Spray Technol. 26 (2017) 902–912, https://doi.org/10.1007/s11666-017-0558-1.

[10] B. Zhang, K. Chen, N. Baddour, Evaluation of solid particle erosion of EB-PVD TBCs under thermal cycling conditions based on a stochastic approach, Coatings 13 (2023), https://doi.org/10.3390/coatings13010156.

[11] M. Shinozaki, T. Clyne, A methodology, based on sintering-induced stiffening, for prediction of the spallation lifetime of plasma-sprayed coatings, Acta Mater. 61 (2013) 579–588, https://doi.org/10.1016/j.actamat.2012.09.079.

[12] R.S. Lima, B.M.H. Guerreiro, M. Aghasibeig, Microstructural characterization and room-temperature erosion behavior of As-deposited SPS, EB-PVD and APS YSZ-based TBCs, J. Therm. Spray Technol. 28 (2019) 223–232, https://doi.org/10.1007/s11666-007-9148-y.

[13] A. Kumar, P.C. Patnaik, K. Chen, Damage assessment and fracture resistance of functionally graded advanced thermal barrier coating systems: experimental and analytical modeling approach, Coatings 10 (2020), https://doi.org/10.3390/coatings10050474.

[14] A. Moteb, K. Chen, Modelling and evaluating thermal conductivity of porous thermal barrier coatings at elevated temperatures, Ceram. Int. 46 (2020) 21939–21957, https://doi.org/10.1016/j.ceramint.2020.04.228.

[15] J. Yan, X. Wang, K. Chen, K.N. Lee, Sintering modeling of thermal barrier coatings at elevated temperatures: a review of recent advances, Coatings 11 (2021), https://doi.org/10.3390/coatings11101214.

[16] B. Zhang, K. Chen, N. Baddour, Crack driving forces of atmospheric plasma-sprayed thermal barrier coatings, Coatings 12 (2022), https://doi.org/10.3390/coatings12081069.

[17] J. Shi, S. Darzens, A. Karlsson, Aspects of the morphological evolution in thermal barrier coatings and the intrinsic thermal mismatch therein, Mater. Sci. Eng. A, Struct. Mater.: Prop. Microstruct. Process. 392 (2005) 301–312, https://doi.org/10.1016/j.msea.2004.09.062.

[18] M.-J. Lee, B.-C. Lee, J.-G. Lim, M.-K. Kim, Residual stress analysis of the thermal barrier coating system by considering the plasma spraying process, J. Mech. Sci. Technol. 28 (2014) 2161–2168, https://doi.org/10.1007/s12206-014-0315-z.

[19] N. Nayebpashaee, S. Seyedein, M. Aboutalebi, H. Sarpoolaky, S. Hadavi, Finite element simulation of residual stress and failure mechanism in plasma sprayed thermal barrier coatings using actual microstructure as the representative volume, Surf. Coat. Technol. 291 (2016) 103–114, https://doi.org/10.1016/j.surfcoat.2016.02.028.

[20] M. Bäker, Finite element simulation of interface cracks in thermal barrier coatings, in: Proceedings of the 21st International Workshop on Computational Mechanics of Materials (IWCMM 21), Comput. Mater. Sci. 64 (2012) 79–83, https://doi.org/10.1016/j.commatsci.2012.02.044.

[21] M. Heidari-Rarani, M. Sayedain, Finite element modeling strategies for 2D and 3D delamination propagation in composite DCB specimens using VCCT, CZM and XFEM approaches, Theor. Appl. Fract. Mech. 103 (2019) 102246, https://doi.org/10.1016/j.tafmec.2019.102246.

[22] G.-R. Li, L.-S. Wang, Durable TBCs with self-enhanced thermal insulation based on co-design on macro- and microstructure, Appl. Surf. Sci. 483 (2019) 472–480, https://doi.org/10.1016/j.apsusc.2019.03.309.

[23] X. Fan, R. Xu, W. Zhang, T. Wang, Effect of periodic surface cracks on the interfacial fracture of thermal barrier coating system, Appl. Surf. Sci. 258 (2012) 9816–9823, https://doi.org/10.1016/j.apsusc.2012.06.036.

[24] L. Cen, W. Qin, Q. Yu, Analysis of interface delamination in thermal barrier coating system with axisymmetric structure based on corresponding normal and tangential stresses, Surf. Coat. Technol. 358 (2019) 785–795, https://doi.org/10.1016/j.surfcoat.2018.12.008.

[25] A. Burov, E. Fedorova, Modeling of interface failure in a thermal barrier coating system on Ni-based superalloys, Eng. Fail. Anal. 123 (2021) 105320, https://doi.org/10.1016/j.engfailanal.2021.105320.

[26] J. Song, S. Li, X. Yang, D. Shi, H. Qi, Numerical study on the competitive cracking behavior in TC and interface for thermal barrier coatings under thermal cycle fatigue loading, Surf. Coat. Technol. 358 (2019) 850–857, https://doi.org/10.1016/j.surfcoat.2018.11.006.

[27] Q. Zhou, L. Yang, C. Luo, F. Chen, Y. Zhou, Y. Wei, Thermal barrier coatings failure mechanism during the interfacial oxidation process under the interaction between interface by cohesive zone model and brittle fracture by phase-field, Int. J. Solids Struct. 214–215 (2021) 18–34, https://doi.org/10.1016/j.ijsolstr.2020.12.020.

[28] L. Min, Z. Wang, X. Hu, D. Zhao, Z. Sun, P. Zhang, W. Yao, T.Q. Bui, A chemo-thermo-mechanical coupled phase field framework for failure in thermal barrier coatings, Comput. Methods Appl. Mech. Eng. 411 (2023) 116044, https://doi.org/10.1016/j.cma.2023.116044.

[29] Y. Xiao, Z. Liu, X. Peng, W. Zhu, Y. Zhou, L. Yang, Spallation mechanism of thermal barrier coatings with real interface morphology considering growth and thermal stresses based on fracture phase field, Surf. Coat. Technol. 458 (2023) 129356, https://doi.org/10.1016/j.surfcoat.2023.129356.

[30] Y. Liu, K. Chen, A. Kumar, P. Patnaik, Principles of machine learning and its application to thermal barrier coatings, Coatings 13 (2023), https://doi.org/10.3390/coatings13071140.

[31] F. Armero, J.C. Simo, A new unconditionally stable fractional step method for non-linear coupled thermomechanical problems, Int. J. Numer. Methods Eng. 35 (1992) 737–766, https://doi.org/10.1002/nme.1620350408.

[32] D. Arndt, W. Bangerth, M. Feder, M. Fehling, R. Gassmöller, T. Heister, L. Heltai, M. Kronbichler, M. Maier, P. Munch, J.-P. Pelteret, S. Sticko, B. Turcksin, D. Wells, The deal.II library, version 9.4, J. Numer. Math. 30 (2022) 231–246, https://doi.org/10.1515/jnma-2022-0054.

[33] M. Bäker, T. Fiedler, J. Rösler, Stress evolution in thermal barrier coatings for rocket engine applications, Mech. Adv. Mater. Modern Proc. 1 (2015) 1–10, https://doi.org/10.1186/s40759-015-0005-2.

[34] H. Hayashi, T. Saitou, N. Maruyama, H. Inaba, K. Kawamura, M. Mori, Thermal expansion coefficient of yttria stabilized zirconia for various yttria contents, Solid State Ion. 176 (2005) 613–619, https://doi.org/10.1016/j.ssi.2004.08.021.

[35] H. Zhao, F. Yu, T.D. Bennett, H.N. Wadley, Morphology and thermal conductivity of yttria-stabilized zirconia coatings, Acta Mater. 54 (2006) 5195–5207, https://doi.org/10.1016/j.actamat.2006.06.028.

[36] F. Tang, J.M. Schoenung, Evolution of Young's modulus of air plasma sprayed yttria-stabilized zirconia in thermally cycled thermal barrier coatings, Scr. Mater. 54 (2006) 1587–1592, https://doi.org/10.1016/j.scriptamat.2006.01.021.

[37] X. Song, M. Xie, F. Zhou, G. Jia, X. Hao, S. An, High-temperature thermal properties of yttria fully stabilized zirconia ceramics, J. Rare Earths 29 (2011) 155–159, https://doi.org/10.1016/S1002-0721(10)60422-X.

[38] S.V. Ushakov, A. Navrotsky, R.J.K. Weber, J.C. Neuefeind, Structure and thermal expansion of YSZ and La2Zr2O7 above 1500 °C from Neutron diffraction on levitated samples, J. Am. Ceram. Soc. 98 (2015) 3381–3388, https://doi.org/10.1111/jace.13767.

[39] S. Guo, Y. Kagawa, Young's moduli of zirconia top-coat and thermally grown oxide in a plasma-sprayed thermal barrier coating system, Scr. Mater. 50 (2004) 1401–1406, https://doi.org/10.1016/j.scriptamat.2004.02.025.

[40] X. Cao, R. Vassen, D. Stoever, Ceramic materials for thermal barrier coatings, J. Eur. Ceram. Soc. 24 (2004) 1–10, https://doi.org/10.1016/S0955-2219(03)00129-8.

[41] M. Eskner, R. Sandström, Mechanical properties and temperature dependence of an air plasma-sprayed NiCoCrAlY bondcoat, Surf. Coat. Technol. 200 (2006) 2695–2703, https://doi.org/10.1016/j.surfcoat.2005.05.035.

[42] G. Di Girolamo, M. Alfano, L. Pagnotta, A. Taurino, J. Zekonyte, R.J.K. Wood, On the early stage isothermal oxidation of APS CoNiCrAlY coatings, J. Mater. Eng. Perform. 21 (2012) 1989–1997, https://doi.org/10.1007/s11665-011-0115-x.

[43] H. Liu, P. Chen, H. Yang, J. Hao, X. Tian, X. He, G. Yu, Processing window and microstructure of NiCoCrAlY coating deposited on cast iron using multilayer laser cladding, J. Spectrosc. 2019 (2019) 1–15, https://doi.org/10.1155/2019/9308294.

[44] H. Takagi, M. Fujiwara, K. Kakehi, Measuring Young's modulus of Ni-based superalloy single crystals at elevated temperatures through microindentation, in: 13th International Conference on the Strength of Materials, Mater. Sci. Eng. A 387–389 (2004) 348–351, https://doi.org/10.1016/j.msea.2004.01.061.

[45] M. Zielińska, M. Zagula-Yavorska, M. Poreba, J. Sieniawski, Thermal properties of cast nickel based superalloys, Arch. Mater. Sci. Eng. 44 (2010) 35–38.

[46] P. Berthod, L. Aranda, Thermal expansion behaviour of ternary Nickel-based, Cobalt-based, and Iron-based alloys containing very high fractions of Carbides, Int. Sch. Res. Not. 2012 (2012) 1–9, https://doi.org/10.5402/2012/750914.

[47] D.W. Kelly, J.P. De, S.R. Gago, O.C. Zienkiewicz, I. Babuska, A posteriori error analysis and adaptive processes in the finite element method: Part I—error analysis, Int. J. Numer. Methods Eng. 19 (1983) 1593–1619, https://doi.org/10.1002/nme.1620191103.

[48] M. Ainsworth, J. Oden, A posteriori error estimation in finite element analysis, Comput. Methods Appl. Mech. Eng. 142 (1997) 1–88, https://doi.org/10.1016/S0045-7825(96)01107-3.

[49] T. Jin, Z. Li, K. Chen, A novel phase-field monolithic scheme for brittle crack propagation based on the limited-memory bfgs method with adaptive mesh refinement, Int. J. Numer. Methods Eng. (2024) e7572, https://doi.org/10.1002/nme.7572.

[50] M.S. Shephard, Linear multipoint constraints applied via transformation as part of a direct stiffness assembly process, Int. J. Numer. Methods Eng. 20 (1984) 2107–2112, https://doi.org/10.1002/nme.1620201112.

[51] W.L. Wood, Control of Crank-Nicolson noise in the numerical solution of the heat conduction equation, Int. J. Numer. Methods Eng. 11 (1977) 1059–1065, https://doi.org/10.1002/nme.1620110703.

[52] D. Britz, O. Østerby, J. Strutwolf, Damping of Crank-Nicolson error oscillations, Comput. Biol. Chem. 27 (2003) 253–263, https://doi.org/10.1016/S0097-8485(02)00075-X.

[53] L. Wang, D. Li, J. Yang, F. Shao, X. Zhong, H. Zhao, K. Yang, S. Tao, Y. Wang, Modeling of thermal properties and failure of thermal barrier coatings with the use of finite element methods: a review, J. Eur. Ceram. Soc. 36 (2016) 1313–1331, https://doi.org/10.1016/j.jeurceramsoc.2015.12.038.

[54] M. Bäker, P. Seiler, A guide to finite element simulations of thermal barrier coatings, J. Therm. Spray Technol. 26 (2017) 1146–1160, https://doi.org/10.1007/s11666-017-0592-z.